Numerical Simulation of Hydrostatic Mountain Waves

J. B. KLEMP AND D. K. LILLY

National Center for Atmospheric Research,[1] Boulder, Colo. 80307

(Manuscript received 13 May 1977, in final form 27 September 1977)

ABSTRACT

A numerical model is developed for simulating the flow of stably stratified nonrotating air over finite-amplitude, two-dimensional mountain ranges. Special attention is paid to accurate treatment of internal dissipation and to formulation of an upper boundary region and lateral boundary conditions which allow upward and lateral propagation of wave energy out of the model. The model is hydrostatic and uses potential temperature for the vertical coordinate. A local adjustment procedure is derived to parameterize low Richardson number instability. The model behavior is tested against analytic theory and then applied to a variety of idealized and real flow situations, leading to some new insights and new questions on the nature of large-amplitude mountain waves. The model proves to be effective in simulating the structure of two observed cases of strong mountain waves with very different characteristics.

1. Introduction

The hydrostatic mountain wave is one of the important wave forms generated in stable air passing over mountainous terrain having a characteristic width of 50 to 200 km. In this range of scale waves are generally not trapped in lower levels of the atmosphere; rather, they propagate energy into the upper troposphere and lower stratosphere. When wave instability and breakdown occur, a substantial drag may be exerted on upper level circulation (Lilly, 1972) and associated clear air turbulence may be hazardous to passing aircraft (Lilly, 1978). At certain locations in the lee of large mountain ranges, intense and damaging surface winds arise when these waves attain large amplitude (Brinkmann, 1974; Klemp and Lilly, 1975; Lilly and Zipser, 1972). By contrast, the classic lee-wave phenomenon, consisting of a train of quasi-periodic waves of wavelength about 10 km extending downstream from a mountain range but largely restricted to the lower and middle troposphere, is essentially nonhydrostatic and is most frequently observed over smaller scale mountains.

In recent years, observational data collected by instrumented aircraft flying over the eastern slope of the Colorado Rocky Mountains (Lilly and Zipser, 1972; Lilly and Kennedy, 1973; Lilly, 1978) and elsewhere (Nichols, 1974) have provided valuable insight into the structure of stationary hydrostatic mountain waves. In addition, statistical evaluation of sounding data by Brinkmann (1974) revealed the general features of the upstream environment during periods in which downslope windstorms were experienced along the Front Range of the Colorado Rockies. This study documented the presence of a layer of increased stability in the lower troposphere while the upstream winds were found to be of order 20 m s^{-1} or greater near and above mountaintop levels but not excessively strong at upper levels. On the basis of these observations, Klemp and Lilly (1975) proposed a mechanism for the generation of large-amplitude mountain waves and associated strong surface winds, derived from a linear analysis of hydrostatic wave motion. This analysis indicated that large-amplitude waves may result from constructive reinforcement of vertically propagating modes which are partially reflected owing to variations of the stability and wind in the ambient atmosphere. Analyses of the optimal structure for simple, multi-layered atmospheres emphasized the importance of a low-level stable layer and indicated that large-amplitude waves are generated when the phase shift of the wave across the troposphere is close to one-half wavelength. Simulations of real data cases using a linear steady-state hydrostatic model demonstrated a strong positive correlation between model results and observations, using the intensity of surface winds as the basis for comparison.

In order to evaluate the importance of finite-amplitude effects and to provide more accurate real data simulations we have developed a nonlinear two-dimensional numerical model for hydrostatic mountain waves. This time-dependent model uses potential temperature for the vertical coordinate and incorporates an upper level damping region to allow upward propagation of wave energy without reflection from

[1] The National Center for Atmospheric Research is sponsored by the National Science Foundation.

0022-4928/78/0078-0107$15.00

the upper boundary. An analysis of this damping layer is presented to define the conditions for which reflection is minimized. Simulations for small and fairly large amplitude mountains are compared to linear and nonlinear analytic solutions for a one-layer atmosphere to test the validity of the numerical representations. For very large amplitudes the flow becomes dynamically unstable. To deal with this case we have developed a procedure for turbulent adjustment which locally increases the Richardson number in unstable layers while conserving total mass and momentum. Simulation of real data is presented for wave motion observed over the lee slope of the Colorado Rockies on two days with strong but very different response characteristics.

The pioneering work on numerical simulation of nonlinear waves was carried out by Foldvik and Wurtele (1967), and has been followed more recently by experiments carried out using two-dimensional versions of three-dimensional mesoscale models by Anthes and Warner (1974), Mahrer and Pielke (1975) and Deaven (1976). Designed to improve mesoscale forecasting, these models have included surface terrain and refined grid resolution with the result that hydrostatic mountain waves may have significant amplitude in model simulations. Because of their dynamical simplicity, mountain wave simulations have been used to demonstrate that the influence of terrain is properly represented. Our analysis indicates, however, that successful mountain wave simulation requires special care in modeling the important physical processes, and the lack of such care may produce misleading results in the wave structures and the momentum and energy transports. The upper boundary condition is a primary problem; in most previous models it is completely reflective, implying that at steady state there should be no vertical flux of energy or momentum. The wave structure is visibly altered by this boundary condition in that no upstream tilt of lines of constant phase should be present in the steady solution. The influence of the reflective upper boundary is not fully realized, however, if simulations are carried out for too short a time for steady state to be approached or if large explicit or implicit computational damping is applied in the domain of interest. In the course of our work we have tried to identify, quantify, and to some extent indicate the resolution of these problem areas.

2. Description of the numerical model

a. Basic equations

We begin with the equations of motion for flow which is time-dependent, two-dimensional and adiabatic. For the wavelength scales of interest we assume that the motion is hydrostatic and that rotational effects are negligible. Potential temperature is used for the vertical coordinate as it has several advantages for the mountain wave problem. In the isentropic framework, the mountain contour is typically a coordinate surface (though it need not be so), vertical advection terms vanish from the equations, and higher resolution is provided in regions of increased stability where the phase of the wave is changing more rapidly. Isentropic coordinates have been used in numerical mountain wave modeling by Krishnamurti (1964) and by Eliassen and Rekustad (1971) for mesoscale mountain waves.

Subject to the assumptions mentioned above, the equations of motion and continuity in (x,Θ) coordinates may be written in a form similar to that given by Lilly and Kennedy (1973):

$$\frac{\partial u}{\partial t}+\frac{\partial}{\partial x}(\tfrac{1}{2}u^2+\Phi)=\nu\frac{\partial^2 u}{\partial x^2}, \tag{1}$$

$$\frac{\partial}{\partial t}\left(\frac{\partial P}{\partial \Theta}\right)+\frac{\partial}{\partial x}\left(u\frac{\partial P}{\partial \Theta}\right)=0, \tag{2}$$

$$g\frac{\partial z}{\partial \Theta}+c_p\left(\frac{\partial T}{\partial \Theta}-T\right)=0, \tag{3}$$

where

$$\Phi=c_pT+gz \quad \text{and} \quad T=\theta_0 e^{\Theta}\left(\frac{P}{P_0}\right)^{R/c_p}. \tag{4}$$

The independent vertical variable is the logarithm of potential temperature, i.e., $\Theta=\ln(\theta/\theta_0)$, where θ_0 is the surface level potential temperature and $P_0=1000$ mb. The right-hand side of the motion equation (1) is an artificial damping term which absorbs wave energy near the upper boundary as described below.

b. Upper dissipative layer

Since our numerical simulations are carried out within a box of finite dimensions, conditions must be specified along boundaries which arbitrarily enclose a portion of the atmosphere. At the lower boundary we assume the mountain contour to be an isentropic surface and thus we need only specify the mountain height $z=h(x)$ at $\Theta=0$.

We believe that special care must be taken in considering the upper boundary condition since it will fundamentally affect the entire solution. Both theory and observations indicate that hydrostatic waves may extend to high altitudes and produce considerable vertical transport of horizontal momentum. For linear, steady-state wave motion, a radiation boundary condition derived by Eliassen and Palm (1960) can be utilized which recognizes that the mountain is the source of wave energy and consequently removes all solutions at the upper boundary which transport wave energy downward. A somewhat simplified and elegant version appropriate to hydrostatic systems has been

presented by Drazin and Su (1975). Unfortunately, it is not evident that this boundary condition can be applied in general to nonlinear systems. Even the concept of radiation becomes more complicated for finite-amplitude waves since partial reflections may occur at any level due to the nonlinear interaction of upward propagating modes. Nevertheless, vertical transport of momentum and energy is apparently a necessary requirement in modeling the real atmosphere.

The solutions presented by Eliassen and Palm (1960) reveal that upward radiation of wave energy is characterized by a particular phase relationship of wave properties for each horizontal wavenumber present in the system. Each Fourier mode, however, is determined by the flow structure across the entire upper boundary. Drazin and Su (1975) show that the Fourier components may be summed and the radiation condition written in terms of a Hilbert transform function. From the results of either analysis, however, it seems impossible for *any* locally specified boundary condition to permit radiation of wave energy. We have analyzed, but do not present here, the flux characteristics of linear solutions using several different upper boundary conditions which involve a local specification of variables, including those used by Mahrer and Pielke (1975) and Deaven (1976). In all cases we have found them to be completely reflective, i.e., the boundary is a nodal point for some physical variable.

In the present investigation we attempt to provide the essence of a radiation condition in the model by including a viscous region beneath the upper boundary, designed to remove the upward propagating wave energy before it can be reflected from the upper surface. In this manner, we avoid having to model the complex mechanisms of wave breakdown and still achieve the desired energy dissipation. To minimize reflections caused by rapid increases in viscosity, the coefficient ν in (1) is increased gradually from zero at the top of the inviscid region, $\Theta=\Theta_1$, to ν_T at the top boundary, $\Theta=\Theta_T$, according to

$$\nu=\nu_T \sin^2\left(\frac{\pi}{2}\frac{\Theta-\Theta_1}{\Theta_T-\Theta_1}\right). \tag{5}$$

Because of the fundamental influence of this damping layer on the wave structure, it is imperative to evaluate its reflection characteristics. An analysis based on linear wave theory is presented below.

After linearizing (1)–(4), the steady-state wave equation can be derived (Klemp and Lilly, 1975) for the perturbation Montgomery potential, $\Phi'=c_pT'+gz'$, yielding

$$\frac{\partial^2\hat{\Phi}}{\partial\Theta^2}+\gamma^2\hat{\Phi}=0, \tag{6}$$

where $\hat{\Phi}$ is a density-weighted Fourier mode defined by

$$\Phi'(x,\Theta)=\left(\frac{\rho_0}{\bar{\rho}}\right)^{\frac{1}{2}}\hat{\Phi}(k,\Theta)e^{ikx}.$$

The overbar refers to the mean state and ρ_0 is a reference density. For an atmosphere with a constant mean wind $\bar{u}$ and stability $N=[g(d\Theta/d\bar{z})]^{\frac{1}{2}}$, the coefficient γ^2 is accurately approximated by

$$\gamma^2=\frac{\beta^2}{\left(1-i\dfrac{k\nu}{\bar{u}}\right)}, \tag{7}$$

where $\beta=g/N\bar{u}$. Beneath the viscous layer, the solution of (6) for a single Fourier mode is given by

$$\hat{\Phi}=C_1e^{i\beta\Theta}+C_2e^{-i\beta\Theta}. \tag{8}$$

For a horizontal wavenumber $k>0$, the term containing C_1 corresponds to the mode propagating wave energy upward while the C_2 term represents the downward propagating mode (Eliassen and Palm, 1960). The ratio $r=|C_2/C_1|$ is then a measure of the reflectivity produced by the upper viscous region. By matching the pressure and displacement height at the top of the inviscid region ($\Theta=\Theta_1$) with the corresponding quantities at the bottom of the viscous layer described by (6), the expression for r becomes

$$r=\left|\frac{C_2}{C_1}\right|=\left|\frac{[\gamma(\Theta_1)+i]\hat{\Phi}(\Theta_1)-i}{[\gamma(\Theta_1)-i]\hat{\Phi}(\Theta_1)+i}\right|, \tag{9}$$

where $\hat{\Phi}(\Theta_1)$ is evaluated from the solution of (6) in the domain $\Theta_1\leqslant\Theta\leqslant\Theta_T$ subject to boundary conditions on the vertical displacement $z'=(\Phi-\partial\Phi/\partial\Theta)/g$, given by

$$\left.\begin{aligned}\hat{\Phi}-\frac{\partial\hat{\Phi}}{\partial\Theta}&=1 \quad \text{at} \quad \Theta=\Theta_1\\ \hat{\Phi}-\frac{\partial\hat{\Phi}}{\partial\Theta}&=0 \quad \text{at} \quad \Theta=\Theta_T\end{aligned}\right\}. \tag{10}$$

The boundary condition at Θ_T corresponds to a rigid lid while the condition at Θ_1 arises from matching. The displacement height at $\Theta=\Theta_1$ has been normalized to unity in deriving (9) and (10) since it cancels identically out of the expression for r. Also, for this analysis, we have ignored the $(\rho_0/\bar{\rho})^{\frac{1}{2}}$ factor in (6). Eqs. (6) and (10), with viscosity ν substituted from (5), are solved numerically by using second-order differencing and inverting the resulting tridiagonal matrix. Fortunately, the depth of the inviscid layer does not influence r and as a result, for the viscosity profile given by (5), r depends only on three dimensionless parameters: $\beta=g/N\bar{u}$, $V=k\nu_T/\bar{u}$ and $D=(\beta/2\pi)(\Theta_T-\Theta_1)$. Here, $\beta/2\pi$ is the ratio of a poten-

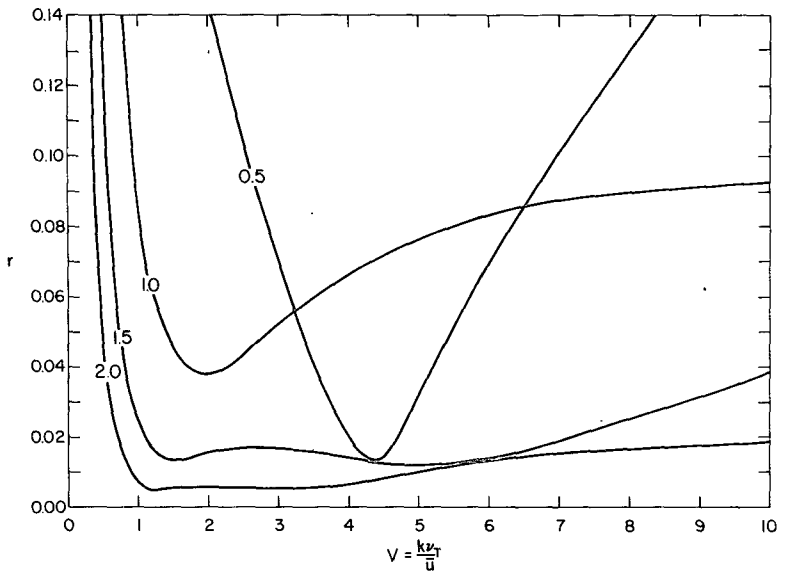

FIG. 1. Reflectivity as a function of V for several viscous layer depths (D=0.5, 1.0, 1.5, 2.0) in which the viscosity profile is given by Eq. (5).

tial temperature scale height g/N^2 to the vertical wavelength $2\pi\bar{u}/N$. The dimensionless viscosity V is an inverse Reynolds number and D is the ratio of the depth of the viscous layer to the vertical wavelength. In addition, for $\beta \gg 1$ (the usual atmospheric case), the solutions for r become independent of β, e.g., for values of β tested between 10 and 100 the reflectivity varied by only several percent.

The reflectivity for $\beta \gg 1$ is plotted in Fig. 1 as a function of V for several thicknesses of the viscous layer. Notice that for a given D and k, r first decreases rapidly with increasing ν_T and then begins to increase. The large reflection at low viscosity results from reflection off the upper boundary due to insufficient damping, while as the viscosity becomes large, its vertical gradient also causes reflection. As the damping layer increases in depth there is a general decrease in reflectivity. It is difficult, however, to interpret the detailed behavior of the reflectivity since the interactions are rather complex. Reflections occur throughout the layer as well as from the upper boundary and the impact of these partial reflections on the inviscid region below depends upon the phase of the reflected mode when it reenters the inviscid

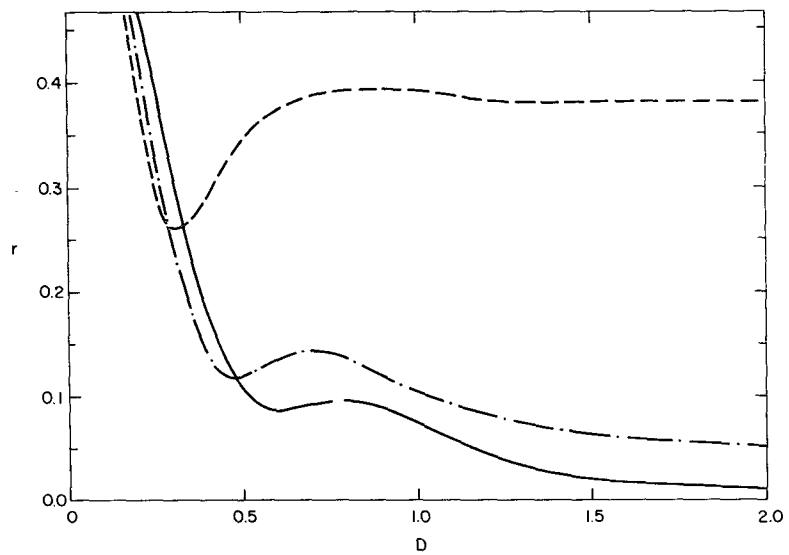

FIG. 2. Average reflectivity in the range $1 \leqslant V \leqslant 10$ as a function of the viscosity profiles: solid line, sine profile (5); dashed-dotted line, linear profile (11); dashed line, constant profile (12).

domain. The net energy and momentum fluxes may be either increased or decreased in the same qualitative manner as in partial reflections caused by layers of differing stability. The complexity of the situation is reflected in Fig. 1 by the variation in the shape of the curves for the different values of D.

If only a single horizontal wavenumber were present in our model, it would be possible to use a relatively thin viscous layer with the viscosity chosen to achieve the minimum possible reflection for that thickness. Unfortunately, we must be concerned with a range of wavenumbers. As the viscous depth decreases, the sensitivity to varying V increases. To summarize this effect Fig. 2 depicts the average reflectivity as a function of D over the range $1 \leqslant V \leqslant 10$. This range was chosen since Fig. 1 suggests that for a one order of magnitude variation in V, this interval yields about the minimum overall reflection. As shown by the solid curve, reflectivity drops to about 10% when the layer is $\frac{1}{2}$ of a vertical wavelength in thickness and drops to 2% at $\frac{3}{2}$ vertical wavelengths. Momentum flux is proportional to the difference of the squares of the coefficients C_1 and C_2 and thus for small r the impact on momentum flux is approximately $2r$.

For comparison, several other viscosity profiles were evaluated. For two of these,

$$\nu = \nu_T \frac{\Theta - \Theta_1}{\Theta_T - \Theta_1}, \tag{11}$$

$$\nu = \frac{\nu_T}{2} \quad \text{for} \quad \Theta > \Theta_1, \tag{12}$$

the reflection coefficient is plotted in Fig. 2, again averaged over the interval $1 \leqslant V \leqslant 10$. Reflection from the constant viscosity layer (12) is high for all D owing to the discontinuity in viscosity at $\Theta = \Theta_1$, while the linear profile (11) produces reflection which is similar to the sine profile (5) but somewhat greater in magnitude. Other viscosity profiles can be devised, such as exponential ones, which yield reflection comparable to that of the sine profile.

To conclude our analysis of the damping layer, we consider the impact of limited numerical resolution on reflectivity to determine the number of vertical grid points required for this region. Using second-order finite differencing in the vertical the average reflectivity in the range $1 \leqslant V \leqslant 10$ is illustrated in Fig. 3 for various n, where n is the number of vertical grid intervals in the viscous domain. The curve for $n = \infty$ corresponds to the profile in Fig. 2. For each value of n, the reflectivity begins to rise when the number of grid points per wave becomes insufficient to resolve the wave structure. In overall terms, about eight grid points per wave (denoted by $\times$'s on the curves) are apparently required to avoid significant reflection due to inadequate resolution. In the present model, most simulations were actually conducted using $n = 20$, $D = 1.5$ and ν_T fixed such that for the dominant wavenumbers in the mountain profile, $V = k\nu_T/\bar{u}$ is near the middle of the range between 1 and 10.

In the above analysis, we have dealt only with damping produced by a horizontal diffusion term in the momentum equation. One could also provide the desired damping by utilizing a Rayleigh viscosity (cf., Houghton and Jones, 1969, and Eliassen and Rekustad, 1971), in which case the term on the right-hand side of (1) would become $-\nu'(u - \bar{u})$, where ν' is an inverse decay time. For this approach the above analysis remains valid if only we replace $V = k\nu_T/\bar{u}$

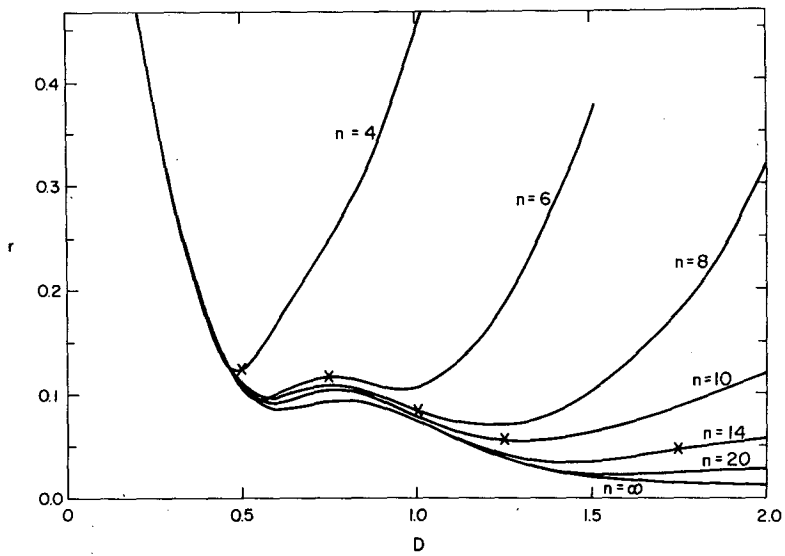

FIG. 3. Average reflectivity in the range $1 \leqslant V \leqslant 10$ as a function of the viscous layer depth D and the number of grid intervals n. The $\times$'s denote locations on the curves corresponding to eight grid intervals per wavelength.

with $V'=\nu_T'/k\bar{u}$. Thus, although the two methods of damping wave energy have inverse behavior with respect to the horizontal wavenumber k, either one can be successfully implemented provided ν_T or ν_T' is appropriately chosen for the desired range of horizontal wavenumbers.

If the viscous layer is effective in damping out upward propagating wave energy, the boundary condition actually specified at $\Theta=\Theta_T$ will have little influence upon the solution. Since a boundary condition is nevertheless required, we have chosen to specify a fixed level for the height of the top Θ surface, i.e., $z(x,\Theta_T)=z_T$. The procedures used to accommodate this boundary condition are discussed in the next section.

c. *Lateral boundary conditions*

In considering the lateral boundaries it must be recognized that for the hydrostatic equations, any conditions specified at these boundaries will, in general, produce an ill-posed problem. As demonstrated by Oliger and Sundström (1976), the characteristic modes may propagate either upstream or downstream depending upon the vertical wavenumber. Consequently, if the vertical mode structure is unresolved a specified set of boundary conditions may be correct for some modes but will be incorrect for others. This result can be readily illustrated for our system of equations by linearizing (1)–(4) and Fourier transforming in the vertical [using $A(x,\Theta)=\sum_l \hat{A}(x,l)e^{il\Theta}$]. In this manner the prognostic equations for the perturbation variables u and $\partial P/\partial\Theta$ can be written in terms of the Fourier coefficients $\hat{u}$ and $\hat{\Phi}$, yielding

$$\left.\begin{aligned} &\frac{\partial\hat{u}}{\partial t}+\bar{u}\frac{\partial\hat{u}}{\partial x}+\frac{\partial\hat{\Phi}}{\partial x}=0\\ &\frac{\partial\hat{\Phi}}{\partial t}+\bar{u}\frac{\partial\hat{\Phi}}{\partial x}+c^2\frac{\partial\hat{u}}{\partial x}=0\end{aligned}\right\}, \tag{13}$$

where $c=g/lN$ represents the intrinsic gravity wave phase speed. By combining these equations, we then obtain

$$\left.\begin{aligned} &\frac{\partial\zeta}{\partial t}+(\bar{u}+c)\frac{\partial\zeta}{\partial x}=0, \quad \zeta=\hat{u}+\frac{1}{c}\hat{\Phi}\\ &\frac{\partial\eta}{\partial t}+(\bar{u}-c)\frac{\partial\eta}{\partial x}=0, \quad \eta=\hat{u}-\frac{1}{c}\hat{\Phi}\end{aligned}\right\}. \tag{14}$$

Notice that the two prognostic equations are now completely decoupled and thus ζ and η are characteristic variables of the system, corresponding to the two gravity wave modes which propagate at speeds $\bar{u}+c$ and $\bar{u}-c$, respectively. The specification of conditions at the lateral boundaries depends upon the direction of propagation of the characteristics, which in turn depends upon the vertical wavenumber l. Thus no boundary formulation will be well posed for all l.

In spite of this theoretical dilemma, a formulation for hydrostatic lateral boundaries was devised which appears to work well for a variety of situations. In deriving lateral boundary conditions, our objective is to specify constraints which minimize the reflection of wave modes propagating to the boundary from the interior and which are well posed. However, since the latter goal cannot always be satisfied, boundary conditions are chosen to be appropriate for wave modes for which $c\gtrsim\bar{u}$ (i.e., modes which can propagate both upstream and downstreeam). For this discussion we assume without loss of generality that $\bar{u}>0$. In this section, discussions will be confined to a presentation of the actual lateral boundary conditions used in the model. An analysis of the reflection caused by these conditions plus comments on the behavior of wave modes having $c<\bar{u}$ (for which these boundary conditions are not properly posed) are included in the Appendix.

In specifying the lateral boundary conditions we attempt to estimate a representative phase speed c^* which is then used to advect disturbances out through the boundaries. Based on Eqs. (14) it is apparent that for $c>\bar{u}$ one boundary condition is required at both the inflow and outflow boundaries. This condition is specified by replacing the motion equation (1) with an expression which advects the horizontal velocity out through the boundary at the estimated phase speed $u+c_0^*$ for outflow and $u-c_i^*$ for inflow. Thus at the outflow boundary,

$$\frac{\partial u}{\partial t}+(u+c_0^*)\frac{\partial u}{\partial x}=0 \tag{15}$$

is solved in conjunction with Eqs. (2)–(4). To maintain numerical stability, the horizontal derivatives in (15) and (2) are computed using a one-sided difference with the boundary point being averaged in time (Elvius and Sundström, 1973).

At the upstream, inflow boundary the corresponding condition becomes

$$\frac{\partial u}{\partial t}+(u-c_i^*)\frac{\partial u}{\partial x}=0. \tag{16}$$

Since we require $u-c_i^*\leqslant 0$ the one-sided spatial derivative in (16) is stably represented in the same manner as in Eq. (15). However, the advection term in (2) cannot be represented using a one-sided difference since for $u>0$ this would constitute a "downstream" difference which is numerically unstable. Consequently, in the equation for $\phi=\partial P/\partial\Theta$ at the inflow boundary the $\partial\phi/\partial x$ term is eliminated by

assuming

$$\frac{\partial \phi}{\partial t} = -u\frac{\partial \phi}{\partial x} - \phi\frac{\partial u}{\partial x} = -(u-c_i^*)\frac{\partial \phi}{\partial x} \tag{17}$$

and solving for $\partial\phi/\partial x$ in terms of $\partial u/\partial x$. Eq. (2) then becomes

$$\frac{\partial \phi}{\partial t} + \left(1 - \frac{u}{c_i^*}\right)\phi\frac{\partial u}{\partial x} = 0, \tag{18}$$

where $\partial u/\partial x$ is written as a one-sided difference, centered in time. For $u \to 0$ this equation is identical to (2) and as $c_i^* \to u$, $\phi = \partial P/\partial\Theta$ approaches a steady state.

These boundary conditions are conceptually similar to a formulation proposed by Orlanski (1976) in which conditions of the form of (15) and (16) were applied to all prognostic variables at both inflow and outflow. His procedure, however, more frequently overspecifies conditions at the boundaries which leads to increased computational mode reflection.

In the above boundary specification c^* (referring either to c_i^* or c_0^*) is a specified phase speed, chosen to be representative of the dominant modes in the system. Of course, a variety of wave modes having different phase speeds will generally be present simultaneously. Thus any chosen value of c^* will be incorrect for certain modes and produce reflection which increases with increasing deviation of each particular c from c^* (see Appendix).

For many applications, it may be possible to reduce boundary reflection to acceptable levels by specifying a constant value of c^* based on the dominant vertical scales of motion (for hydrostatic flow, c is inversely proportional to the vertical wavenumber l). In the application of similar lateral boundary conditions in a nonhydrostatic cloud model by Klemp and Wilhelmson (1978), tests revealed that little boundary reflection arose using a fixed value of $c^* = 30$ m s^{-1}. In the present simulations as steady state is approached $u + c_0^* \to 0$ in (15) and $u - c_i^* \to 0$ in (16). These asymptotic values cannot be imposed during the transient response, however, without causing large-amplitude reflections since u would then be fixed at both boundaries for all time.

To provide estimates of the phase speeds which have the correct behavior at steady state we have implemented a variation of Orlanski's (1976) procedure for computing c^* which requires

$$\left.\begin{aligned} u + c_0^* &= -\frac{u_t}{u_x} \quad \text{at outflow} \\ u - c_i^* &= -\frac{u_t}{u_x} \quad \text{at inflow} \end{aligned}\right\}. \tag{19}$$

In our grid system, the derivatives on the right-hand side of (19) are centered one-half grid interval in from the boundary at time level $t - \Delta t$. Using this approach c_i^* and c_0^* converge to the proper value as $u_t \to 0$.

Although Orlanski computed separate values of c^* at each grid point along a lateral boundary for each variable, we have chosen here to simply vertically average the calculated values of $u + c_i^*$ along the respective boundaries and use these averaged values at each point along the boundaries. In this manner we smooth out large variations in c^* which occur from one grid point to the next along a boundary. Since c^* is at best a rough approximation to the actual phase speeds, this procedure is intended to provide a ballpark estimate which approaches the correct value at steady state. At inflow we require $u - c_i^* \leqslant 0$, and thus if a positive value of $u - c_i^*$ is computed it is adjusted back to zero prior to the vertical averaging. Similarly, we enforce $u + c_0^* \geqslant 0$ at outflow.

The lateral boundary formulations described above are admittedly somewhat arbitrary, but in the absence of practical theoretical guidance a pragmatic attitude has been adopted. The analysis presented in the Appendix suggests that little reflection occurs for wave modes having phase speeds near c^* and that even if c^* is poorly chosen, reflection coefficients are likely to remain substantially less than unity. If modes are also present having $c < u$ an outflow boundary condition overspecifies the problem for these modes; by using the condition (15) these modes tend to produce small-amplitude reflections into short-wavelength computational modes which do not seriously distort the physical solution. Although this analysis does not investigate the numerical stability of the boundary conditions, in practice they produce no observable instability in the model. Computations were carried out for up to 7000 time steps for small-amplitude disturbances with no damping (either physical or computational) in the system without producing instabilities or a systematic drift of boundary values.

In dealing with the lateral boundaries, we found no significant advantage in utilizing a stretched horizontal grid near the boundaries, such as that applied by Mahrer and Pielke (1975). For finite-amplitude simulations, disturbances such as upstream propagating blocks and downstream traveling jumps can alter the mean state of the atmosphere. With a small amount of stretching the boundary problem is not reduced, while with large stretching disturbances propagating into the continuously expanding mesh reach a point where inadequate resolution produces reflections which appear to alter flow in the central portion of the domain. Consequently, for this model we maintained a constant horizontal grid spacing.

d. Finite-difference equations

The prognostic equations (1) and (2) are numerically integrated using centered differences accurate to second-order in time and space. Because of the particular form of these equations, staggering the mesh in time substantially enhances computational efficiency. At each time level all variables are defined on the same spatial grid except for $\partial P/\partial\Theta$, which is vertically staggered. At all even time levels the locations of the grid points are horizontally shifted by one-half grid interval from their positions at the odd time levels. In this framework the finite-difference formulation of (1)–(3) becomes

$$\delta_{2t}u+\delta_x(\tfrac{1}{2}u^2+c_pT+gz) =\nu\left[\delta_{\frac{1}{2}x}(\delta_{\frac{1}{2}x}u)-\left(\frac{\Delta t}{\Delta x}\right)^2\delta_t(\delta_t u)\right], \quad (20)$$

$$\delta_{2t}\frac{\partial P}{\partial\Theta}+\delta_x\left(u\frac{\partial P}{\partial\Theta}\right)=0, \quad (21)$$

$$\delta_\Theta P=\frac{\partial P}{\partial\Theta}, \quad (22)$$

$$g\delta_\Theta z+c_p(\delta_\Theta T-\bar{T}^\Theta)=0, \quad (23)$$

where the finite-difference operators are defined as

$$\left.\begin{aligned}\delta_{n\xi}A(\xi)&=\frac{1}{n\Delta\xi}[A(\xi+\tfrac{1}{2}n\Delta\xi)-A(\xi-\tfrac{1}{2}n\Delta\xi)]\\ \bar{A}^{n\xi}&=\tfrac{1}{2}[A(\xi+\tfrac{1}{2}n\Delta\xi)+A(\xi-\tfrac{1}{2}n\Delta\xi)]\end{aligned}\right\}, \quad (24)$$

with A being the appropriate dependent variable, ξ the independent variable and $n\Delta\xi$ the number of grid intervals over which the operation takes place. The finite-difference approximation of $\partial^2u/\partial x^2$ in (20) corresponds to the DuFort-Frankl representation in the time-staggered mesh.

For the initial conditions, we again are faced with a somewhat arbitrary choice. For this model we have chosen to begin the numerical simulation by inserting the mountain terrain into an initially undisturbed atmosphere having a specified state which is independent of x. Since an abrupt change in the surface contour excites large-amplitude transient gravity waves, the mountain height is gradually increased over a number of time steps (usually 500) to minimize these disturbances. A similar procedure was used by Deaven (1976). Although these initial conditions are not physically realistic our primary interest here is in the long time, nearly steady-state solution which should not depend strongly upon the initial development.

Numerical integration of the above equations proceeds in the following manner. First the variables u and $\partial P/\partial\Theta$ are stepped forward in time from t to $t+\Delta t$ using the leapfrog scheme described by (20) and (21). Because of the time staggering the lateral boundary conditions [(15) for outflow and (16) and (18) for inflow] are applied only at the even time steps since at the odd steps the variables are defined one-half grid interval in from the boundary. Eqs. (22) and (23) must then be vertically integrated subject to the boundary conditions $z(x,0,t)=h(x)$ and $z(x,\Theta_T,t)=z_T$. This is accomplished by defining

$$\left.\begin{aligned}P^{t+\Delta t}&=P^*(x,\Theta)+\epsilon(x)P_0\\ \text{and}\qquad z^{t+\Delta t}&=z^*(x,\Theta)+\epsilon(x)z_\epsilon(x,\Theta),\end{aligned}\right\} \quad (25)$$

$$P^*=P^{t-\Delta t}(x,\Theta_T)+\int_{\Theta_T}^{\Theta}\frac{\partial P^{t+\Delta t}}{\partial\Theta}d\Theta. \quad (26)$$

Thus P^* and z^* denote the pressure and height fields at $t+\Delta t$ assuming the pressure at the top of the domain did not change during the time step. We then seek to solve for ϵ which represents the dimensionless pressure change at the top of the domain during that time step. Linearizing (4) for small ϵ such that

$$T^{t+1}=T^*\left(1+\epsilon\frac{R}{c_p}\frac{P_0}{P^*}\right),\quad T^*=\theta_0e^\Theta\left(\frac{P^*}{P_0}\right)^{R/c_p} \quad (27)$$

allows (23) to be separated into two equations:

$$\left.\begin{aligned}\delta_\Theta z^*&=\frac{c_p}{g}[\overline{T^*}^\Theta-\delta_\Theta T^*]\\ \delta_\Theta z_\epsilon&=\frac{RP_0}{g}\left[\overline{\left(\frac{T^*}{P^*}\right)}^\Theta-\delta_\Theta\left(\frac{T^*}{P^*}\right)\right]\end{aligned}\right\}. \quad (28)$$

These equations are solved by integrating (26) vertically downward to obtain P^*, and then (28) upward using P^*, T^* and the boundary conditions $z^*(x,0)=h(x)$ and $z_\epsilon(x,0)=0$. To satisfy the upper boundary condition, we require

$$\epsilon=\frac{z_T-z^*(x,\Theta_T)}{z_\epsilon(x,\Theta_T)},$$

which finally allows us to obtain P^{t+1} and z^{t+1} from (25). At this point all variables have been stepped forward to time $t+\Delta t$ and the procedure described above is repeated for the next time step. To initiate this scheme we begin at $t=0$ with one forward time step before switching to leapfrog steps. Time splitting was not encountered in any of the simulations.

In the above finite-difference equations, incorporating a time-staggered mesh requires no additional spatial or temporal averaging. As a result, we generate a solution at each grid point which is identical to

the corresponding unstaggered solution in half the computer time and with half as much storage. The only difference is that at any particular time the solution exists at half as many grid points which reduces the resolution for display purposes. As steady state is approached, however, this deficiency can be eliminated by combining the solutions at two consecutive time steps to double the spatial grid-point density.

e. Turbulence adjustment procedure

As finite-amplitude mountain waves propagate upward through the atmosphere, they may become unstable at certain levels, dissipate a portion of their energy, and in the process remove momentum from the mean flow. Although the mechanisms for turbulent wave breakdown are not completely understood, observations of large-amplitude mountain waves along the Front Range of the Colorado Rockies (Lilly and Kennedy, 1973; Lilly, 1978) indicate that this dissipation may be generated by Kelvin-Helmholtz type instabilities. Within certain regions of the flow, the local Richardson number Ri drops below the critical value of 0.25 and instability ensues. In the subsequent process of turbulent mixing, conditions within an unstable layer are altered such that the local Richardson number increases above the critical value and stability is reestablished. For our model, incorporation of turbulence adjustment processes will be based on this mechanism.

We assume, therefore, that when $\mathrm{Ri}<\mathrm{Ri}_c$ (which can be arbitrarily specified) turbulence develops which produces mixing and increases the local Richardson number to $\mathrm{Ri}_a \geqslant \mathrm{Ri}_c$. In parameterizing this adjustment we assume that the total mass and momentum are conserved, that heat and momentum are similarly redistributed (i.e., turbulent Prandtl number of unity), and that only the unstable layer and immediately adjacent levels are affected by the adjustment process.

Although total mass must obviously remain unchanged, justification for requiring conservation of total momentum may not be clear. In a breaking gravity wave there may, in fact, be a removal of momentum. However, this removal occurs through a vertical flux away from the region of wave breakdown, not due to outright disintegration of momentum within the unstable layer. To amplify this point, consider the momentum equation in Θ coordinates which is derived by combining (1)–(3) for inviscid flow:

$$\frac{\partial}{\partial t}\left(u\frac{\partial P}{\partial \Theta}\right)+\frac{\partial}{\partial x}\left[(u^2+RT)\frac{\partial P}{\partial \Theta}\right]+\frac{\partial}{\partial \Theta}\left(gP\frac{\partial z}{\partial x}\right)=0. \quad (29)$$

At steady-state, this equation can be horizontally integrated (assuming conditions far upstream and downstream remain undisturbed) to yield

$$\frac{\partial M}{\partial \Theta}=0, \quad \text{where} \quad M=-\int_{-\infty}^{\infty} P\frac{\partial z}{\partial x}dx \quad (30)$$

has the form of surface wave drag but here represents the vertical flux of horizontal momentum across each isentropic surface. Thus, in the absence of dissipation the momentum within a layer is unaltered since the downward vertical flux through that level is constant. However, when turbulent mixing occurs a vertical gradient in M is established which produces a net vertical flux of momentum away from the layer. The purpose of the adjustment process is to allow this gradient in M to form and thus transfer momentum away from the turbulent layer, either to some other turbulent layer or to the ground. The adjustment term itself should conserve momentum.

The assumption that heat and momentum mix similarly is perhaps not ideal since the eddy Prandtl number probably should be somewhat less than unity. It is very convenient in the adjustment scheme, however, and it is doubtful that the simplification will cause any serious error. Finally, the assumption that mixing remains localized is certainly a plausible requirement for all variables, except possibly pressure, owing to the small scales expected for the mixing processes. Furthermore, in order to conserve mass and satisfy specified boundary conditions, it seems essential for pressure also. In connection with the concept of localized mixing, adjustment processes take place only in the vertical. Since the horizontal mesh spacing is large compared to that in the vertical for a hydrostatic model it is assumed that the generation and decay of turbulence all occurs within a horizontal mesh distance.

The details of the parameterization will be developed in the context of the particular grid structure and finite-difference methods used in our model. For a different numerical framework, the same procedures should apply, although certain details may be somewhat altered. We begin after all variables have been computed at a new time level by calculating the local Richardson number for layers between each successive Θ level. The Richardson number is thus defined between levels Θ_k and Θ_{k+1} (at the point where $\partial P/\partial \Theta_{k+\frac{1}{2}}$ is located) by the expression

$$\mathrm{Ri}_{k+\frac{1}{2}}=\frac{g\delta_\Theta z}{(\delta_\Theta u)^2}=\frac{g\Delta\Theta(z_{k+1}-z_k)}{(u_{k+1}-u_k)^2}. \quad (31)$$

If $\mathrm{Ri}_{k+\frac{1}{2}}<\mathrm{Ri}_c$ we adjust the Richardson number back to Ri_a by changing z_{k+1} and z_k in the numerator of (31). We do not alter the denominator, which is consistent with the assumption of unit Prandtl number. Defining δ as the adjustment operator, the alteration

of $\mathrm{Ri}_{k+\frac{1}{2}}$ back to Ri_a occurs via the expression

$$\delta z_{k+1}-\delta z_k=\frac{\mathrm{Ri}_a-\mathrm{Ri}_{k+\frac{1}{2}}}{g\Delta\Theta}(u_{k+1}-u_k)^2. \tag{32}$$

If the adjustments are made symmetrically, such that $\delta z_{k+1}=-\delta z_k$ then the finite-difference hydrostatic equation (23) could not be satisfied unless the pressure was altered at all levels above or below z_k, thus violating the requirement for conservation of mass. We therefore seek to allocate the adjustment between z_k and z_{k+1} such that (32) is satisfied and that grid values are altered only at levels k and $k+1$, which is consistent with our assumption of localized mixing. To insure that the hydrostatic balance is maintained, adjustments to the unstable layer must be such that

$$\left.\begin{aligned}(1-\tfrac{1}{2}\Delta\Theta)\delta T_{k+2}-(1+\tfrac{1}{2}\Delta\Theta)\delta T_{k+1}&\\ =-(g/c_p)(\delta z_{k+2}-\delta z_{k+1})&\\ (1-\tfrac{1}{2}\Delta\Theta)\delta T_{k+1}-(1+\tfrac{1}{2}\Delta\Theta)\delta T_k&\\ =-(g/c_p)(\delta z_{k+1}-\delta z_k)&\\ (1-\tfrac{1}{2}\Delta\Theta)\delta T_k-(1+\tfrac{1}{2}\Delta\Theta)\delta T_{k-1}&\\ =-(g/c_p)(\delta z_k-\delta z_{k-1})&\end{aligned}\right\}. \tag{33}$$

Eqs. (33) are just the hydrostatic equation (23) evaluated at three adjacent levels. Confining the adjustments to levels k and $k+1$ we require that $\delta T_{k+2}=\delta z_{k+2}=\delta T_{k-1}=\delta z_{k-1}=0$. Eqs. (32) and (33) then form a set of four equations in four unknowns which have the solution

$$\left.\begin{aligned}\delta z_{k+1}&=\frac{\mathrm{Ri}_a-\mathrm{Ri}_{k+\frac{1}{2}}}{2g\Delta\Theta}(u_{k+1}-u_k)^2(1+\tfrac{1}{2}\Delta\Theta)\\ \delta z_k&=-\frac{\mathrm{Ri}_a-\mathrm{Ri}_{k+\frac{1}{2}}}{2g\Delta\Theta}(u_{k+1}-u_k)^2(1-\tfrac{1}{2}\Delta\Theta)\\ \delta T_{k+1}&=-\delta T_k=-\frac{\mathrm{Ri}_a-\mathrm{Ri}_{k+\frac{1}{2}}}{2c_p\Delta\Theta}(u_{k+1}-u_k)^2\end{aligned}\right\}. \tag{34}$$

Using (4) and (22), the appropriate adjustments to P_{k+1}, P_k, $\partial P/\partial\Theta_{k-\frac{1}{2}}$, $\partial P/\partial\Theta_{k+\frac{1}{2}}$ and $\partial P/\partial\Theta_{k+\frac{3}{2}}$ are then made.

Finally, in order to assure conservation of momentum, we must arrange that the integral $\int u(\partial P/\partial\Theta)d\Theta$ remains constant, which requires that

$$\begin{aligned}\delta[&(u_{k+2}+u_{k+1})(P_{k+2}-P_{k+1})\\ &+(u_{k+1}+u_k)(P_{k+1}-P_k)\\ &+(u_k+u_{k-1})(P_k-P_{k-1})]=0.\end{aligned} \tag{35}$$

Since the adjustments are expected to be small compared to the initial values, it is appropriate to linearize this expression. In addition, we specify that $\delta u_{k+1}=\delta u_k$ so the Richardson number will not be altered, and set $\delta u_{k+2}=\delta u_{k-1}=0$.

Solving (35) we then find

$$\delta u_{k+1}=\delta u_k=\frac{(u_{k+2}-u_k)\delta P_{k+1}+(u_{k+1}-u_{k-1})\delta P_k}{P_{k+2}+P_{k+1}-P_k-P_{k-1}} \tag{36}$$

which completes the adjustment solution.

The net effect of the adjustment procedure is to increase the physical thickness and mass of a dynamically unstable layer between Θ_k and Θ_{k+1} and correspondingly to decrease both the static stability and the wind shear across the layer. After the adjustments are made, P_k will have been altered (usually decreased) in the layers just above and below that of the initial instability since the thickness and mass of these layers have been slightly decreased. Thus, to be rigorous, a second test on $\mathrm{Ri}-\mathrm{Ri}_c$ should be made for the column and possibly a further adjustment. In practice, however, we find that it is sufficient to adjust only once and thus secondary effects are adjusted on subsequent time steps. Numerical simulations were conducted with $\mathrm{Ri}_c=\mathrm{Ri}_a=0.25$, causing supercritical regions to be continuously adjusted to a Richardson number of 0.25. Since adjustment is required at most at only a small fraction of the grid points, this procedure is not computationally expensive.

To illustrate how this adjustment procedure might operate, consider the following example:

$$z_{k+1}-z_k=400\text{ m},\quad \theta_k=297\text{ K},\quad \Delta\theta=6\text{ K}$$
$$u_{k+1}-u_k=20\text{ m s}^{-1},\quad P_k=800\text{ mb}.$$

For these conditions $\mathrm{Ri}=0.2$ and $P_k-P_{k+1}=40$ mb. Assuming $\mathrm{Ri}_c=\mathrm{Ri}_a=0.25$, from (32) $\delta z_{k+1}-\delta z_k=100$ m. The requirement of mass conservation in (34) produces a 0.5 m lifting of the mean height of the layer such that $\delta z_{k+1}=50.5$ m and $\delta z_k=-49.5$ m. However, the mean pressure of the layer is slightly increased since from (34) and (4) we obtain $\delta P_{k+1}=-4.72$ mb while $\delta P_k=5.00$ mb. Eq. (36) provides an adjustment in u to account for the difference in momentum of the air entrained into the layer from above and below. If we assume that $P_{k+1}-P_{k+2}=P_{k-1}-P_k=40$ mb and that the shearing layer extends downward but not upward, so that $u_{k+2}-u_k=20$ m s^{-1} and $u_{k+1}-u_{k-1}=30$ m s^{-1}, then (36) yields $\delta u_k=\delta u_{k+1}=-0.33$ m s^{-1}.

3. Comparisons with analytic solutions

Before describing numerical simulations of real flow situations, it is instructive to analyze several simplified cases in order to determine how accurately the model represents the basic features of mountain waves and to provide an indication of how nonlinear effects influence the wave structure. For this purpose, comparisons of model results against linear and nonlinear analytic solutions provide a rigorous test of the accuracy of the numerical model formulation.

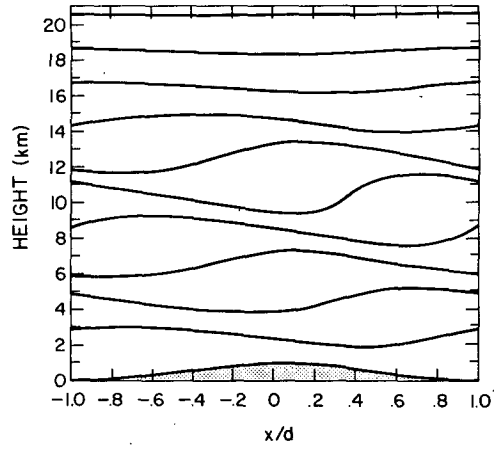

FIG. 4. Steady-state potential temperature surfaces for $h=500$ m. Sinusoidal mountain contour (with perturbations amplified by a factor of 2) at $t\bar{u}/d=20$.

For simplicity we shall consider an initially uniform atmospheric structure which is isothermal and has a horizontal wind speed of 20 m s^{-1}. As an illustration of the nature of the solutions produced by the model, Fig. 4 displays the steady-state displacement of the constant potential temperature coordinate surfaces throughout the integration domain for flow over a 500 m sinusoidal mountain contour with periodic lateral boundaries. Here perturbations have been amplified by a factor of 2 for better visualization of the wave structure. At steady state, these material surfaces coincide with streamlines of the fluid motion. The flow is directed from left to right and the upper absorbing layer, described in section 2(b), begins at a height of 10 km. The simulation utilizes 40 grid intervals in the vertical and 10 in the horizontal which is sufficient to accurately resolve the wave structure. The horizontal scale has been rendered dimensionless with respect to the characteristic mountain half-width d, since for steady, inviscid flow the horizontal length scale can be factored out of the governing equations (1)–(4) and thus influences the solution only by providing a horizontal scaling factor. The dimensionless integration time is defined by u_0t/d, and the time step is fixed at 0.01.

These stationary waves display certain basic features which are characteristic of the hydrostatic wave solutions generated by this model. Lines of constant wave phase tilt upstream with height, indicating a negative correlation between horizontal and vertical velocity and thus a downward flux of horizontal momentum. Wave amplitude generally increases with height, which is consistent with the result from linear theory that it should grow in proportion to the inverse square root of density. In the dissipative layer above 10 km the waves are gradually damped with height and vanish near the upper boundary.

To provide a quantitative evaluation of the model performance, we shall begin by comparing the model results against linear theory for this same uniform inviscid atmosphere flowing over a continuously sinusoidal mountain contour. The linear, second-order wave equation in (x,Θ) coordinates for this case is represented by (6) in the previous section with γ^2 given to a good approximation by

$$\gamma^2=\frac{g^2}{N^2\bar{u}^2}=\frac{c_p\bar{T}}{\bar{u}^2}. \tag{37}$$

Here we have chosen the (x,Θ) framework for the linear analysis since the lower boundary, being a constant θ surface, is treated without approximation. (A comparison of linear solutions using different vertical coordinates is discussed later in this section.)

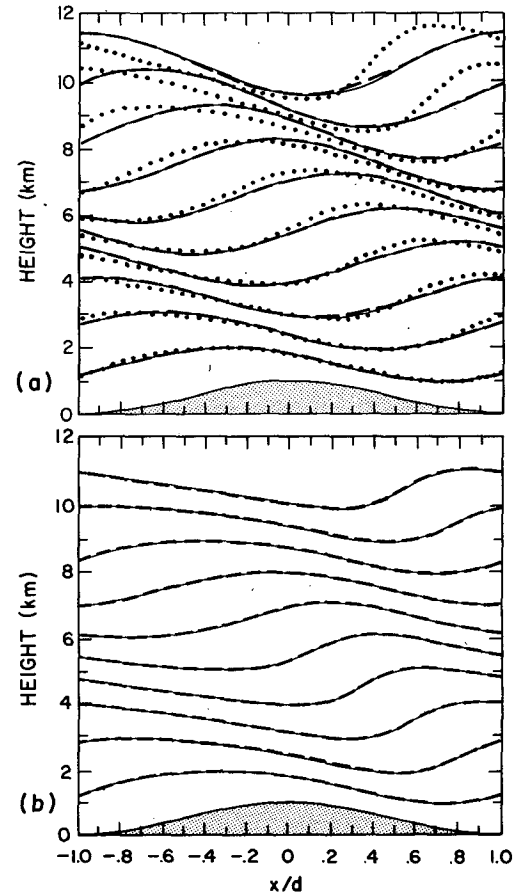

FIG. 5a. Comparison of linear analytic and numerical solutions for displacement of potential temperature surfaces for sinusoidal mountain contour with $h_0=100$ m: solid line, numerical solution at $t\bar{u}/d=20$; dashed line, linear analytic solution. Also, the numerical solution for $h_0=500$ m is shown in dotted lines.

FIG. 5b. Numerical and analytic Boussinesq solutions for $h_0=750$ m: solid line, numerical solution at $t\bar{u}/d=20$; dashed line, analytic nonlinear solution. Perturbations have been amplified to normalize the mountain height to 1 km.

For the one-layer atmosphere under consideration the wave equation (6) has constant coefficients since γ^2 in (37) is constant. The solution is further simplified in that the mountain profile corresponds to a single Fourier mode. This solution, derived for the displacement height, where $gz=\Phi-\partial\Phi/\partial\Theta$, with a radiative upper boundary is given by

$$z(x,\Theta)=\frac{h_0}{2}\left\{1+e^{c_p\Theta/2R}\cos\left[\pi x+\frac{(c_p\bar{T})^{\frac{1}{2}}}{\bar{u}}\Theta\right]\right\}, \quad (38)$$

where h_0 denotes the peak-to-trough amplitude of the sinusoidal mountain.

The corresponding numerical simulation was obtained using the same grid structure as described for the solution in Fig. 4. In Fig. 5a the solid lines depict the streamlines generated by the nonlinear numerical model for a mountain height of 100 m, which is small enough that we would expect the flow field to be very nearly linear. The corresponding analytic solution given by (38) is plotted in dashed lines with the perturbations in both cases amplified by a factor of 10 in order to better visualize the comparison. The analytic and numerical solutions are almost indistinguishable, indicating that numerical resolution is sufficient and that the upper damping region (not shown in the figure) accurately simulates the desired radiation condition. For contrast the solution for $h_0=500$ m is also displayed in Fig. 5a with the dotted lines and with the perturbations amplified by a factor of 2. (This is the same solution as shown in Fig. 4.) Here nonlinear effects are clearly significant, as evidenced by the pronounced steepening of the wave with height.

Nonlinear steady-state analytic solutions can be obtained for hydrostatic Boussinesq flow if the upstream stability and wind profiles are independent of height based on Long's (1953) equation

$$\frac{\partial^2\delta}{\partial z^2}+\frac{N^2}{\bar{u}^2}\delta=0, \quad (39)$$

where δ is the displacement of a streamline about its undisturbed level. Although (39) is linear, complications arise in satisfying the lower boundary condition since the mountain contour does not correspond to a coordinate surface. As a result numerical procedures are usually implemented to obtain solutions for particular terrain profiles. Recently, however, Lilly and Klemp (1978) found that through a simple transformation of the vertical coordinate, closed form solutions to (39) can be derived for any desired mountain contour. By defining $\zeta=z-h(x)$, $h(x)$ being the mountain profile, this solution is given by

$$\delta(x,\zeta)=h(x)\cos l\zeta+f(x)\sin l\zeta, \quad (40)$$

where $l=N/\bar{u}$. To satisfy the radiation condition, $f(x)$ is computed using a generalization of the procedure proposed by Drazin and Su (1975) which for linear solutions yields

$$f(x)=f_L(x)=\frac{1}{\pi}P\int_{-\infty}^{\infty}\frac{h(x')}{x'-x}dx', \quad (41)$$

where P refers to the principal value of the integral. For nonlinear solutions the corresponding condition (Lilly and Klemp, 1978) becomes

$$f(x)=f_L(x)-\frac{1}{\pi}\int_{-\infty}^{\infty}\{1-\cos l[h(x')-h(x)]\}\frac{h(x')dx'}{x'-x}$$
$$-\frac{1}{\pi}\int_{-\infty}^{\infty}\sin l[h(x')-h(x)]\frac{f(x')dx'}{x'-x}. \quad (42)$$

Eq. (42) represents an integral equation for f which can be solved iteratively by choosing $f=f_L$ as a first guess in the last term on the right-hand side of (42), solving for the improved estimate for f, and then repeating the procedure. Evaluating these integrals numerically, an accurate profile for f can be obtained with only several iterations.

In order to compute a numerical solution for comparison with (40) from our model, we transform the Boussinesq equations in (x,z) coordinates to the (x,Θ) framework which yields

$$\left.\begin{aligned}&\frac{\partial u}{\partial t}+\frac{\partial}{\partial x}(\tfrac{1}{2}u^2+\Phi)=\nu\frac{\partial^2 u}{\partial x^2}\\&\frac{\partial}{\partial t}\left(\frac{\partial z}{\partial\Theta}\right)+\frac{\partial}{\partial x}\left(u\frac{\partial z}{\partial\Theta}\right)=0\\&\frac{\partial\Phi}{\partial\Theta}=-gz\end{aligned}\right\}, \quad (43)$$

where $\Phi=c_p(T-\bar{T})-g\Theta z$. Integrating equations (43) to a steady state for a sinusoidal mountain with $h_0=750$ m yields the solution depicted in Fig. 5b by the solid lines. (Here again the perturbations have been amplified for visual purposes to normalize the mountain height to 1 km.) The dashed lines in Fig. 5b correspond to the analytic solution from (40) and (42), and again reveal a good agreement of the results. For Boussinesq flow nonlinear contributions to the solution produce maximum steepening of the wave at odd multiples of a half-wavelength above the ground and disappear at the even multiples (Smith, 1977). These results are clearly evident in (42).

As mentioned in the previous section, the vertical flux of horizontal momentum for steady, inviscid mountain waves should be independent of height. This behavior for the numerical solution is examined in Fig. 6 for the $h_0=100$ m (peak to trough) sinusoidal mountain whose streamlines are exhibited in Fig. 5a.

In the inviscid region below 10 km the momentum flux computed by integrating $P\partial z/\partial x$ over one period, corresponds to the linear analytic solution

$$M=(\pi/4)\rho_0 h_0^2 \frac{g\gamma}{\gamma^2+\left(1-\frac{c_p}{2R}\right)^2}\approx(\pi/4)\rho_0 N\bar{u}h_0^2 \quad (44)$$

indicated by the dashed line in Fig. 6. In the dissipative region above 10 km the momentum flux is continuously diminished owing to viscous dissipation of the wave energy. The good agreement in the inviscid domain below verifies that this wave absorption is achieved with little reflection. The small wiggles in the profile arise since M is not exactly conserved in the finite-difference equations.

For the 500 m mountain (Fig. 5a) the momentum flux is almost exactly a factor of 25 greater than the 100 m case, indicating that nonlinearities have not altered the momentum flux, even though the wave structure has been noticeably affected. This result is consistent with the analysis by Lilly and Klemp (1978) which indicates that for a symmetric mountain the momentum flux associated with the nonlinear Boussinesq solution (40) and (42) does not deviate significantly from that computed from linear theory until the wave amplitudes are close to overturning.

We conclude our discussion of flow over a single Fourier component of a mountain terrain by describing the results when the barrier height was increased to 1 km. For this case, steady solutions could not be obtained: small-scale instabilities gradually developed (even though the minimum Richardson number remained greater than 0.25) and grew continuously in amplitude until the numerical solution was destroyed. By sufficiently reducing the mesh resolution we found that these were apparently high-wavenumber physical instabilities of the governing equations. Fourier decomposition of the flow field revealed pairs of high-wavenumber modes growing in amplitude probably through resonant interaction with the fundamental mode. The growth of secondary modes due to triad interactions is well documented. In fact, Hasselmann (1967) proved that all undamped modes are destabilized through the growth of infinitesimal disturbances due to resonant wave interactions. Davis and Acrivos (1967) identified the instability and derived expressions for the growth rates of the unstable modes for periodic waves in a channel. For flow over an isolated mountain, we would expect this instability to be less significant than that encountered for the sinusoidal profile since a single mountain will consist of a series of horizontal wavenumbers, each having an amplitude less than the mountain height.

As a final test of our model using linear theory, we examine the numerical solution for flow of this same initially isothermal atmosphere having a constant (20 m s^{-1}) horizontal wind speed past a small-amplitude bell-shaped mountain. This case allows us to evaluate the simulation of a flow field containing a rather broad range of horizontal wavenumbers and for which the lateral boundaries are nonperiodic. To obtain this solution, the same grid structure was utilized as in the example presented in Fig. 4, with the dimensionless domain width $L=6$ and $z_T=20$ km. To insure linearity of the numerical solution the mountain height was set at $h_0=10$ m.

The linear analytic solution is obtained from (6) with the lower boundary condition for each Fourier mode $\hat{\Phi}$ derived from the Fourier transform of the mountain profile

$$z(x,0)=\frac{b^2h_0}{x^2+b^2} \quad (45)$$

and a radiating upper boundary to eliminate downward propagating modes. In (6), γ^2 is again given by (37) and the resulting linear solution has the form

$$z(x,\Theta)=bh_0e^{c_p\Theta/2R}\frac{b\cos\gamma\Theta-x\sin\gamma\Theta}{x^2+b^2} \quad (46)$$

and

$$u(x,\Theta)=Nh_0b\gamma e^{c_p\Theta/2R}\frac{\{\gamma x-b(1-c_p/2R)\}\cos\gamma\Theta+\{b\gamma+(1-c_p/2R)x\}\sin\gamma\Theta}{\{\gamma^2+(1-c_p/2R)^2\}(x^2+b^2)}$$

which, for $\gamma\gg1$, can be simplified to

$$u(x,\Theta)=Nbh_0e^{c_p\Theta/2R}\frac{b\sin\gamma\Theta+x\cos\gamma\Theta}{x^2+b^2}. \quad (47)$$

The steady-state streamlines generated by the time-dependent numerical model (amplified by a factor of 50 for visualization purposes) are plotted in Fig. 7 for the central portion of the flow field. (Here we have set the mountain half width d equal to 2b.) For comparison the analytic solution given by (46) is also represented in the plot by the dashed lines. To analyze the momentum transport, M is computed on the basis of (30), using (45) and (47) with $P=-\bar{p}(\bar{u}u+gz)$. Somewhat surprisingly, the result is identical to the value of M given by (44). In other words the momentum flux produced by a bell-shaped mountain between $-\infty$ and $+\infty$ is the same as that generated by one cycle of a sinusoidal contour having the same peak-to-trough height. In addition the

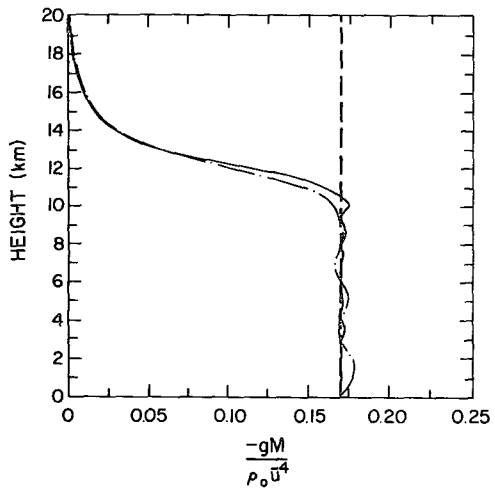

FIG. 6. Momentum flux profiles for $h_0=100$ m: dashed line, analytic solution (44) for both sinusoidal and bell-shaped mountains; solid line, numerical solution for sinusoidal mountain; dashed-dotted line, numerical solution for bell-shaped mountain.

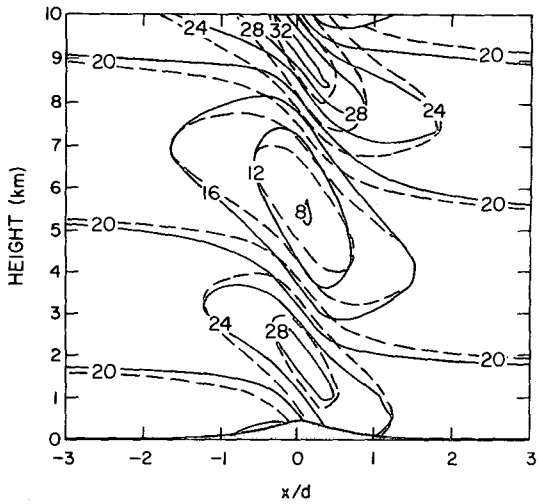

FIG. 8. Comparison of linear solutions for horizontal velocity in (x,θ) and (x,z) coordinates: solid line, (x,θ) solution; dashed line, (x,z) solution. Labels denote velocity (m s^{-1}) for both solutions.

momentum flux for the bell mountain is independent of b since the hydrostatic solution is independent of the horizontal length scale. The momentum flux profile produced in the numerical simulation (amplified by 10^2 so it represents $\hat{M}$ for a 100 m mountain) is plotted with a dashed line in Fig. 6, and again $\hat{M}$ is close to the analytic value in the inviscid region below 10 km. The good agreement between analytic and computed solutions demonstrated in Figs. 6 and 7 confirms our expectations that the nonperiodic lateral boundary formulations do not distort the results, that the upper damping region can effectively absorb wave energy over a range of horizontal wavenumbers, and that the finite-difference resolution is sufficient to accurately model the flow.

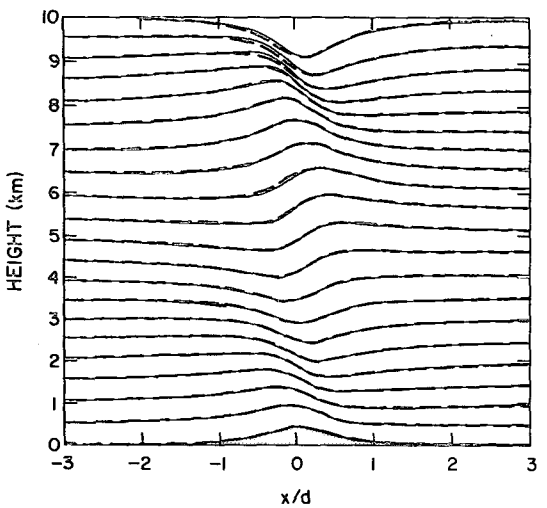

FIG. 7. Comparison of linear analytic and numerical solutions for displacement of potential temperature surfaces for bell-shaped mountain. Perturbations have been amplified to normalize the mountain height to 500 m (solid line, numerical solution at $t\bar{u}/d=50$; dashed line, linear analytic solution).

It is of interest to note the difference between the linear solution computed in (x,θ) coordinates and the more conventional solution derived in the (x,z) framework (Alaka, 1960). For the displacement height, both approaches yield the result given by (46) since $\gamma\Theta$ is equivalent to $(N/\bar{u})z$. Similarly the expression for horizontal velocity from the (x,z) analysis has the same form as (47). There is, however, an important difference between the two horizontal velocity fields. In the (x,z) system the u profile for a given value of the vertical coordinate z is located at that mean height $\bar{z}$. On the other hand, in the (x,θ) framework, for a given value of the vertical coordinate the u profile is located along a constant θ surface, which is itself displaced in the vertical. As the displacement amplitude of the perturbation increases the difference between the two approaches becomes more pronounced. This effect is illustrated in Fig. 8 where the linear horizontal velocity field associated with the flow in Fig. 7 is plotted both from the (x,θ) system and from an (x,z) analysis. Notice that in the (x,Θ) solution the perturbation surface velocity is very nearly antisymmetric about $x=0$ as it should be, while in the (x,z) result the asymmetry is more significant since the surface profile is actually located at $z=0$. Also, near the top of the domain, differences are accentuated where the spacing between streamlines is markedly decreased.

The favorable comparisons of our model results with analytic solutions do not, of course, insure against numerical errors arising in more complex situations, nor do they prove the superiority of isentropic coordinates to other terrain following systems.

However, quantitative documentation of the model accuracy for these simplified cases provides a solid base from which we can proceed to more complicated simulations with some confidence that the fundamental processes are being properly represented.

4. Nonlinear solutions for multilayer atmospheric structures

Having tested the model behavior against analytic solutions, we now turn to large-amplitude cases where nonlinear effects and vertically varying atmospheric structures play significant roles in determining the wave structure. Through numerical modeling, nonlinear mountain waves can be simulated for a variety of atmospheric conditions, most of which cannot be obtained currently from nonlinear analytic solutions. At the same time, analyses based upon numerical modeling are hindered because the solutions are generated for a specific set of conditions, and it is often difficult to identify the important forcing mechanisms and the extent to which results may be generalized to other (even similar) situations. Recognizing this dilemma, we shall concentrate on results which appear to be rather typical of certain classes of atmospheric cases.

For finite-amplitude simulations, certain adjustments in the computational procedure are required which were not necessary for linear situations. For example, the turbulence adjustment scheme described in Section 2e is incorporated to prohibit the minimum Richardson number from dropping below a critical value of 0.25. In addition, a small amount of damping is required for large-amplitude solutions to stabilize nonlinear numerical and possibly physical instabilities (recall the instabilities described in Section 3 for a 1 km sinusoidal mountain). This is accomplished by fixing $\nu=\nu_0$ below $\Theta=\Theta_1$, in (1) at the smallest value which is sufficient to maintain stability. For the simulations conducted ν_0 was held within the range $0\leqslant \nu_0/(u_0 d)\leqslant 0.01$ with values chosen in the lower half of this range for all but the very strongest cases. To estimate the magnitude of damping produced by this term, consider its effect in the steady-state linear wave equation given by (6). To avoid confusion due to the time staggered grid, we define $\Delta x'=\frac{1}{2}\Delta x$ which then represents the horizontal grid interval in the corresponding unstaggered system. Using second-order horizontal finite-differencing as outlined in (20) and (21) the coefficient γ^2 becomes

$$\gamma^2=\frac{\beta^2}{1-i\dfrac{k\nu_0}{u_0}\left(\dfrac{2}{k\Delta x'}\tan\dfrac{k\Delta x'}{2}\right)}. \tag{48}$$

For $k\nu_0/u_0\ll 1$, the upward radiating solution to (6) is damped in the vertical by a factor of

$$\exp\left[-\frac{k\nu_0}{2u_0}\left(\frac{2}{k\Delta x'}\tan\frac{k\Delta x'}{2}\right)\beta\Theta\right]. \tag{49}$$

As an example, assume there is a one-half wavelength phase shift between the mountain and the tropopause at $\Theta=\Theta_1$, ($\beta\Theta_1=\pi$). Then, for a disturbance of horizontal wavelength $4\Delta x'$ (i.e., $k=\pi/2\Delta x'$) this coefficient at the tropopause becomes

$$\exp\left(-\frac{\pi\nu_0}{\Delta x' u_0}\right).$$

With $\Delta x'/d=0.2$ and $\nu_0/u_0 d$ at its maximum value of 0.01, the wave amplitude is reduced by about 14%. Of course, this effect is reduced for longer wavelength components of the flow and for smaller values of $\nu_0/u_0 d$.

Using the procedures described above numerical damping can be adjusted to suppress instability with minimal influence on the wave structure. In this regard, numerical schemes which contain inherent computational damping are undesirable since this damping is difficult to regulate, and may have substantial impact on the results. For example, Mahrer and Pielke (1975) use a first-order upstream differencing scheme for advection terms in the prognostic equations. Using their finite-difference representations the coefficient γ^2 in the linear steady wave equation (with no explicit damping terms present) becomes

$$\gamma^2=\left(\frac{\beta}{1-i\tan\frac{1}{2}k\Delta x'}\right)^2. \tag{50}$$

By comparing (50) with (48) for $k\Delta x'\ll 1$ it is clear that this coefficient produces the same damping coefficient as (49) with $\nu_0/u_0 d=\Delta x'/d$. In Mahrer and Pielke's simulations $\Delta x'/d=0.3$ which is 30 times greater than our maximum value of $\nu_0/u_0 d$. For a $4\Delta x$ wave (corresponding to 40 km in their model) the damping factor one-half vertical wavelength above ground is $e^{-\pi/2}$, which causes an 80% reduction in wave amplitude. This large damping reduces the reflective effect of the upper boundary since most of the wave energy is dissipated throughout the troposphere and doesn't reach this boundary.

The effect of a highly damped numerical model is somewhat similar to that of bringing our damping layer down to the surface. A tilted wave with upward energy and downward momentum transports is produced, although these transports diminish rapidly with height. The predicted value of momentum flux at the surface is then similar to that of an atmosphere with constant stability equal to that near the surface. In the presence of a tropopause and/or other sharp changes in stability or wind, this prediction will generally be incorrect, by as much as an order

of magnitude in some cases, as shown by Blumen (1965) and Klemp and Lilly (1975). For example, consider a two-layer atmosphere in which the stability in the upper stratospheric layer is twice that in the lower tropospheric layer. Based on linear analysis the momentum flux will increase by a factor of 16 as the thickness of the lower layer changes from an odd multiple of one-quarter vertical wavelength in thickness to an even multiple (Klemp and Lilly, 1975). With significant damping present in the lower layer this sensitivity would not be realized.

In computing the momentum flux, adjustments are also required for finite-amplitude waves, since M is uniquely defined only within the linear framework. For nonlinear situations ambiguities arise in that M is based on the correlation of perturbation variables, yet the mean state itself is being altered, making identification of the perturbation portion uncertain. If the flow far upstream or downstream is altered, then the momentum flux as defined by (30) is no longer constant with height and different formulations for M lead to different results [e.g., Eq. (30) is no longer equivalent to the horizontal integral of $\bar{\rho}u'w'$]. Since the $\bar{\rho}u'w'$ correlation is commonly used for momentum flux calculations, we make our formulation for M consistent with this approach by noting that from the linear steady-state equation, $u'w' = -\Phi'\partial z'/\partial x$. Thus, for the numerical model in the θ framework,

$$M(\theta) = -\bar{\rho}\int_{-L}^{L} (\Phi - \bar{\Phi})\frac{\partial z}{\partial x}\,dx. \tag{51}$$

In seeking the best estimate for M, we allow $\bar{\Phi}$ to be a linear function of x, using a least-squares fit at each θ level. This approach minimizes vertical oscillations in the M profile which arise if $\bar{\Phi}$ is defined to be constant at each level and is also similar to the approach used in observational analysis (Lilly, 1978).

In order to present a representative sample of nonlinear model results we have selected simulations derived for a simple, but not unrealistic, two-layer atmospheric structure. This atmosphere consists of a troposphere extending up to 10 km in which the temperature lapse rate is a constant 6°C km^{-1}, with $T_0 = 280$ K and an isothermal stratosphere between 10 and 20 km which also serves as the damping layer as described in Section 2b. The horizontal wind is

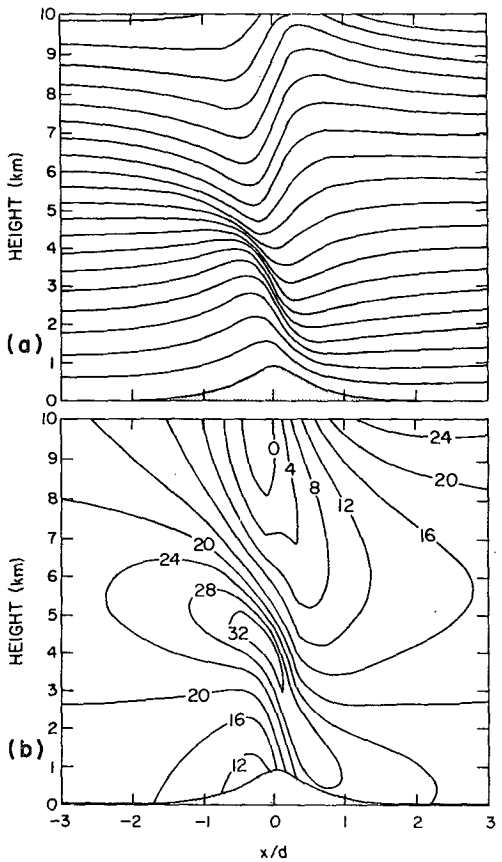

FIG. 9. Linear numerical solution for two-layer atmosphere at $t\bar{u}/d = 50$. (a) Displacement of potential temperature surfaces; (b) contours of horizontal velocity (m s^{-1}).

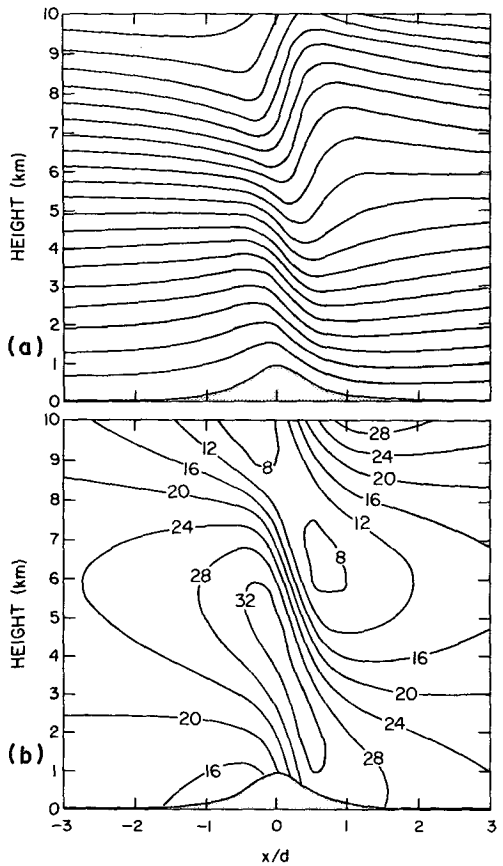

FIG. 10. Numerical solution with $h_0 = 1000$ m for two-layer atmosphere at $tu_0/d = 50$. (a) Displacement of potential temperature surfaces; (b) contours of horizontal velocity (m s^{-1}).

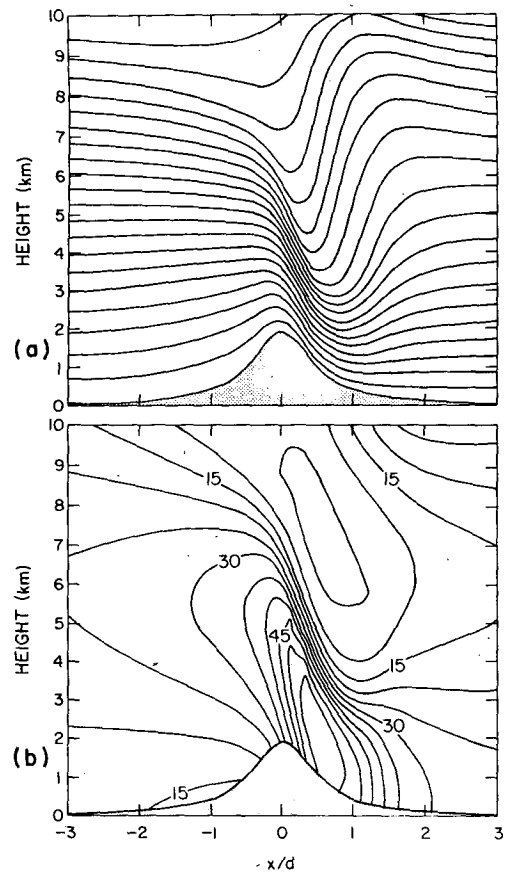

FIG. 11. As in Fig. 10 except with $h_0=2000$ m and at $tu_0/d=25$.

initially set independent of height at 20 m s^{-1} and the bell-shaped mountain contour is described by (45) with $b=d/2$.

For this set of initial atmospheric conditions, the linear and nonlinear steady-state solutions are illustrated in Figs. 9 and 10 for $h_0=1000$ m. The linear solution was obtained by setting $h=1$ m and amplifying the resulting perturbations by 1000. This procedure insures that nonlinear interactions in the equations are insignificant. These figures depict the streamline and horizontal velocity fields throughout the troposphere, having omitted the upper damping layer and the region $3<|x/d|<6$ in which perturbations only continue their smooth decay with increasing distance from the mountain.

Comparing Figs. 9 and 10 we see that under these conditions, the linear and nonlinear results are at least qualitatively similar. The horizontal velocity maximum is comparable in both simulations and occurs in the vicinity of one-quarter of a vertical wavelength above the mountain. The wave structure in the upper troposphere is similar although some steepening of the wave has occurred in the nonlinear case. The most noticeable difference occurs in the lower troposphere where in the linear solution streamlines are packed closely together in the region of strong shear owing to the change in phase of the wave with height. Since by continuity the horizontal velocity is inversely proportional to the distance between streamlines this spacing is clearly inconsistent with the velocity field. In the nonlinear case the deficiency is removed through maintenance of an increased interval between streamlines. In these solutions, the flow field becomes almost independent of x at large horizontal distances from the mountain, and thus moving the location of the inflow boundary further upstream has little effect on the results.

Increasing the mountain amplitude to 2 km produces a wave structure, depicted in Fig. 11, in which nonlinear effects are clearly significant. The large-amplitude wave induces strong acceleration of flow at low levels in the lee of the mountain; and the horizontal velocity maximum is displaced downward and into the lee of the mountain while its perturbation amplitude is increased by a factor of 3 over the value for a 1 km mountain.

For the two-layer atmosphere under consideration the linear phase shift of the wave between the mountain and the tropopause is close to one vertical wavelength. According to linear theory (Blumen, 1965; Klemp and Lilly, 1975), the momentum flux achieved when the lower layer is an integer multiple of a half-wavelength in thickness is the same as that produced by a single-layer atmosphere with the stability of the upper layer. Consequently, the linear dimensionless momentum flux for this case should be just slightly less than the value of 17 computed for the isothermal atmosphere in the previous section after scaling up

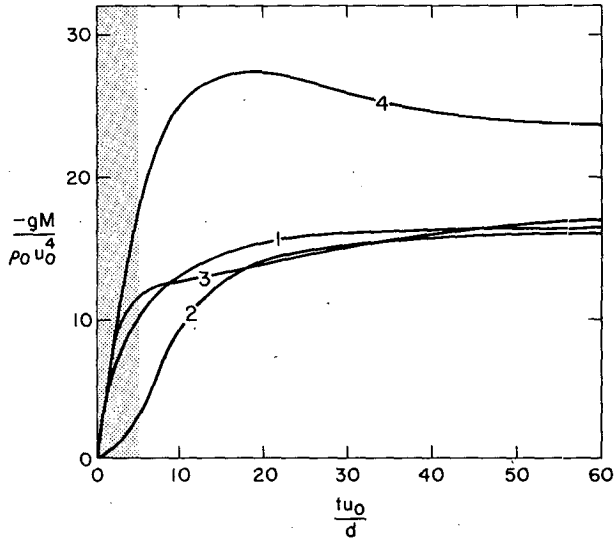

FIG. 12. Time-dependent behavior of momentum flux profiles for two-layer atmosphere: 1—surface flux for linear solution; 2—flux at 10 km level for linear solution; 3—surface flux for $h_0=1000$ m; 4—surface flux for $h_0=2000$ m divided by a factor of 4. The shaded area indicates the duration over which the mountain is introduced.

the mountain height from 100 m to 1 km (see Fig. 6). In Fig. 12 the linear momentum flux is plotted as a function of time for the surface level (curve 1) and the tropopause level (curve 2) which is just below the damping layer. The curves converge in time to a dimensionless value of 16 which is consistent with the one-layer result. As expected, the upper level momentum flux develops more slowly than near the surface and here a dimensionless time of about 30 is required before the flux profile is nearly constant with height. This corresponds to the time it takes the air to pass across the mountain (of width $2d$) 15 times. When nonlinearities are present, this development may take place even more slowly. Curve 3 depicts the evolution of surface level momentum flux for the 1 km mountain. Although the momentum flux increases more slowly than the linear response, it eventually achieves about the same magnitude. Increasing the mountain height to 2 km causes substantial enhancement of the momentum flux. Curve 4 in Fig. 12 represents the momentum flux for $h_0=2$ km after dividing the actual flux by a factor of 4 in order to facilitate comparison with the profiles for $h_0=1$ km. As the wave structure develops a maximum flux occurs at $tu_0/d=25$ which is nearly double the linear value for a mountain of the same height. Fig. 11 corresponds to this dimensionless time of 25. With further increase in time the vertical momentum flux gradually drops off and the wave appears to shift slightly upstream. To test the influence of reflection from the lateral boundaries, this simulation was recomputed with the same grid resolution but with the boundaries twice as far from the mountain ($L=\pm 12$). For this case the flow field displayed little change though the more sensitive momentum flux was decreased by about 10%.

The increased momentum flux for the 2 km mountain above the linear value is consistent with Lilly and Klemp's (1978) analytic solutions for a one-layer atmosphere which indicate that the momentum flux is substantially increased at wave amplitudes which are nearly overturning. However, it is also possible that nonlinear contributions to the momentum flux are more significant for the two-layer atmosphere or perhaps that partial reflections due to the turbulence adjustment processes amplify the response.

The time-dependence of momentum flux profiles depicted in Fig. 12 provides an indication of the time required to obtain steady solutions. For comparison, Deaven (1976) introduces the mountain over the first hour of integration and then analyzes results at 3 h, corresponding to $tu_0/d=5.4$. This time should be associated with an early stage of wave development. For his case, $u_0=15$ m s^{-1} and $d=2b=30$ km. Similarly Mahrer and Pielke (1975) raise the mountain over 2 h and display their results at 4 h, for which $tu_0/d=7.2$. In both cases, however, further wave development would be restricted by their large computational damping.

5. Comparison with observational data

In seeking to compare model simulations against observational data for situations involving large mountain wave amplitude, one finds the choice of cases rather limited. Such observations have been collected by flying one or more instrumented aircraft through the standing wave system to determine the structure and the associated vertical flux of horizontal momentum. Unfortunately, it has proven difficult to schedule and conduct aircraft flights during strong episodes owing to the sporadic nature of the event and its typically short duration. Furthermore, strong accompanying surface winds and severe air turbulence frequently inhibit flight operations.

The most spectacular case to be observationally well-documented along the eastern slope of the Colorado Rockies occurred on 11 January 1972. On this day Boulder, Colo., experienced one of its most severe downslope windstorms with surface winds gusting as high as 120 mph (55 m s^{-1}). Two periods of several hours each contained frequent gusts over 100 mph (45 m s^{-1}). Investigation of the associated mountain waves by Lilly and Zipser (1972) and Lilly (1978) revealed the presence of the powerful wave system depicted in Fig. 13.

To numerically simulate this case we must specify initial temperature and horizontal wind profiles which characterize the undisturbed atmosphere. Recognizing that any such initialization derived from real data is somewhat ambiguous, we have chosen those profiles based upon the National Weather Service 1700 MST sounding (see Fig. 14) taken at Grand Junction, Colo., some 300 km west of Boulder. This sounding time is appropriate for the upper level portion of the observations in Fig. 13.

For modeling purposes ground level on the upwind side of the mountain is taken to be the same as that in the lee. Consequently, the base of the upwind profiles is set at 830 mb which is just slightly above the elevation of Grand Junction. From 830 mb to the tropopause at 190 mb the potential temperature and the westerly wind component were entered into the model at approximately 100 mb intervals. Above the tropopause, the atmosphere was specified to be isothermal with a constant wind of 30 m s^{-1}. Absorption of wave energy takes place within this upper layer, which extends to 25 km. For establishing upstream profiles, the pressure and wind are interpolated to the potential temperature coordinate surfaces using cubic splines.

Instead of attempting to specify the detailed mountain terrain we have chosen a simpler, bell-shaped contour with the same elevation change (2 km) as that between the Continental Divide and the plains im-

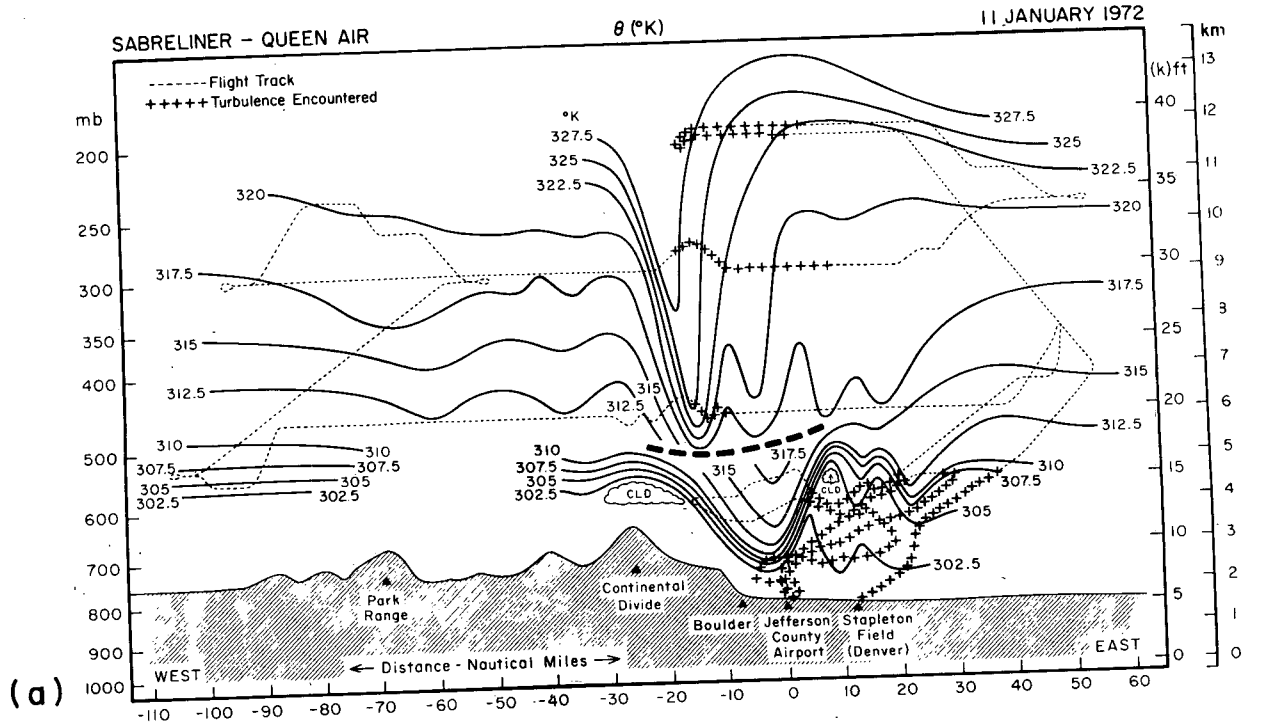

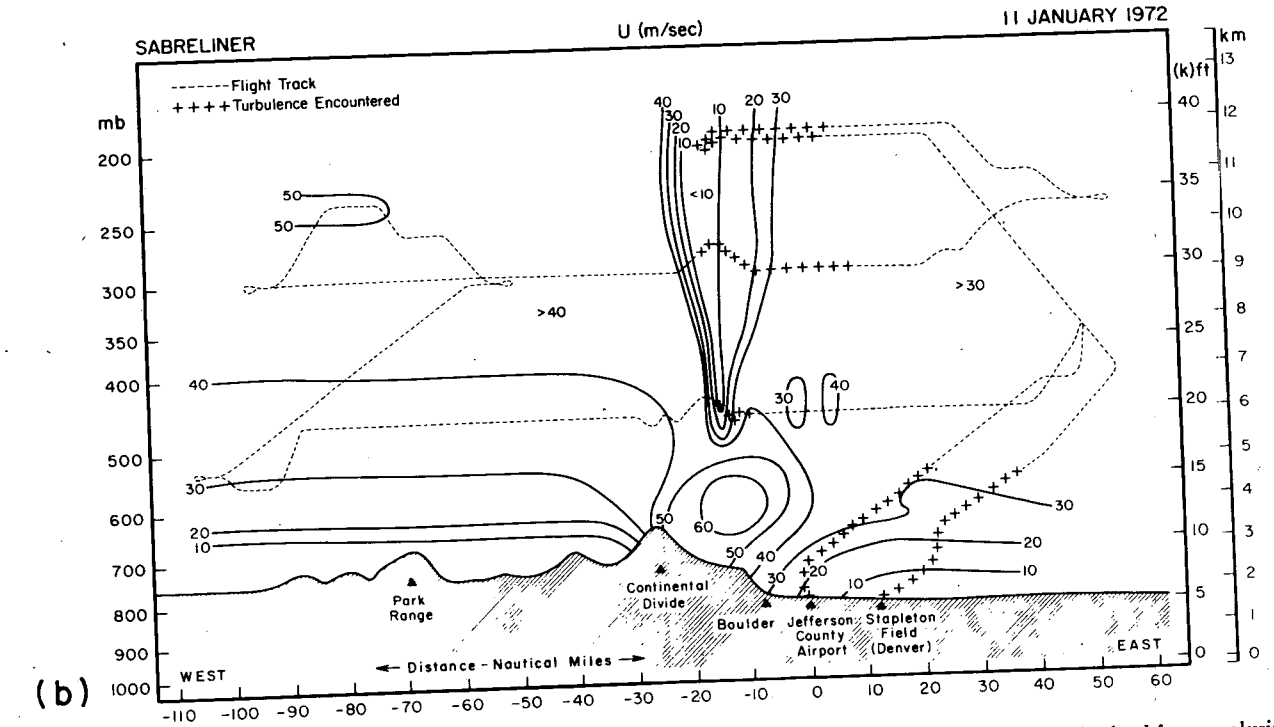

FIG. 13a. Cross section of the potential temperature field (K) along an east–west line through Boulder, as obtained from analysis of the Queen Air and Sabreliner data on 11 January 1972. Data above the heavy dashed line are from the Sabreliner, taken between 1700 and 2000 MST, while those below this line are primarily from the Queen Air taken from 1330 to 1500. Flight tracks are indicated by the dashed lines, except for crosses in turbulent portions. For further details, see Lilly and Zipser (1972).

FIG. 13b. Contours of horizontal velocity (m s^{-1}) along the same cross section as in (a), as derived from the Sabreliner data only. The analysis below 500 mb was partially obtained from vertical integration of the continuity equation, assuming two-dimensional steady-state flow.

mediately to the east. Because of the upstream influence and partial blocking of low level flow, the detailed shape of the upwind side of the mountain was not found to have a strong influence upon the solution.

The numerical solution for the 11 January 1972 data integrated to a steady-state result is shown in Fig. 15. Here the potential temperature and horizontal velocity fields have been plotted throughout the troposphere and out to the lateral boundaries at $x/d=\pm 6$ in order to depict the model results on a scale which is similar to the observations in Fig. 13. In Fig. 15a the streamlines reflected by the potential temperature surfaces show the presence of a large-amplitude wave standing over the lee slope of the mountain which is rather similar to the observed wave in Fig. 13a. In these two figures, the low-level stable layer is identified by the decreased vertical spacing between adjacent θ surfaces. Upwind of the mountain, the stable layer has been lifted through upstream influence and maintains a fairly constant elevation. Thus even though a bell-shaped mountain contour was specified, low-level flow develops the ramp-like structure consistent with the actual terrain. Although complete blocking cannot occur in the framework of this model since $\partial P/\partial\Theta$ must be finite and $u\partial P/\partial\Theta$ is constant with x in the steady state, the low-level flow upstream of the mountain can be significantly retarded and thus produces a similar effect. Immediately in the lee of the mountain, the stable layer recovers rapidly as in the observed flow and appears similar to a hydraulic jump. In addition the computed phase shift of the wave across the troposphere agrees with the observations, as evidenced by the similar shape of the upper level streamlines.

Turning to the horizontal wind fields in Figs. 13b and 15b, we find the basic flow structure is again

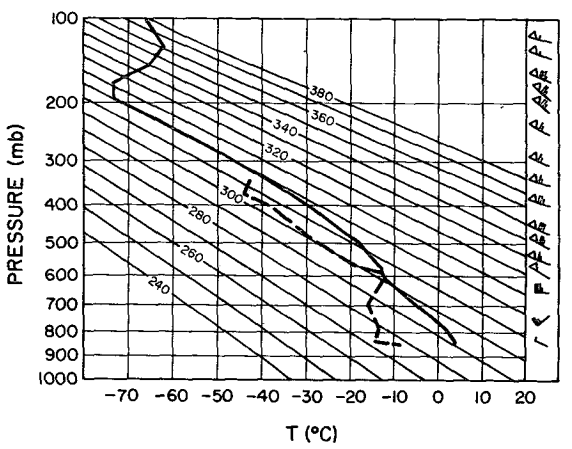

FIG. 14. 1700 MST Grand Junction sounding (solid line, temperature; dashed line, dew-point temperature). The oblique axis indicates potential temperature levels. Wind barbs at the right represent the wind speed (kt) and wind direction using standard meteorological notation.

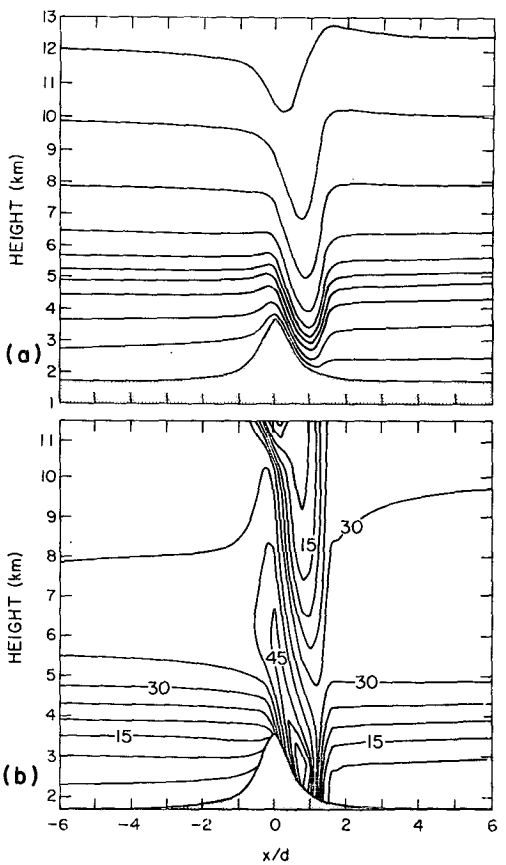

FIG. 15. Numerical simulation of 11 January 1972 case. (a) Displacement of potential temperature surfaces; (b) contours of west wind component (m s^{-1}). Maximum surface velocity in the lee of the mountain is 55 m s^{-1}.

well-represented by the model. Strong winds are predicted just above the lee slope while a low velocity trough extends through the upper portion of the wave. Note that the mean west wind at mid-levels is somewhat less than that recorded by the instrumented aircraft. This difference probably arises because the wind direction was west-northwest and thus the Grand Junction station is about 150 km south of the actual trajectory for air passing over the Continental Divide west of Boulder.

Data from the 20 000 and 30 000 ft flight legs were used to estimate the momentum flux associated with this large-amplitude wave. Assuming 200 km for the length of the traverses the average of the two computed values corresponds to a momentum flux of 47 dyn cm^{-2} (4.7 Pa). For comparison, the flux generated by the model simulation using the same averaging distance is about 30 dyn cm^{-2}.

In a previous investigation (Klemp and Lilly, 1975) we simulated this same case using a linear steady-state wave model. Although the linear solution also produced a large-amplitude response, certain differences between the two approaches are noteworthy.

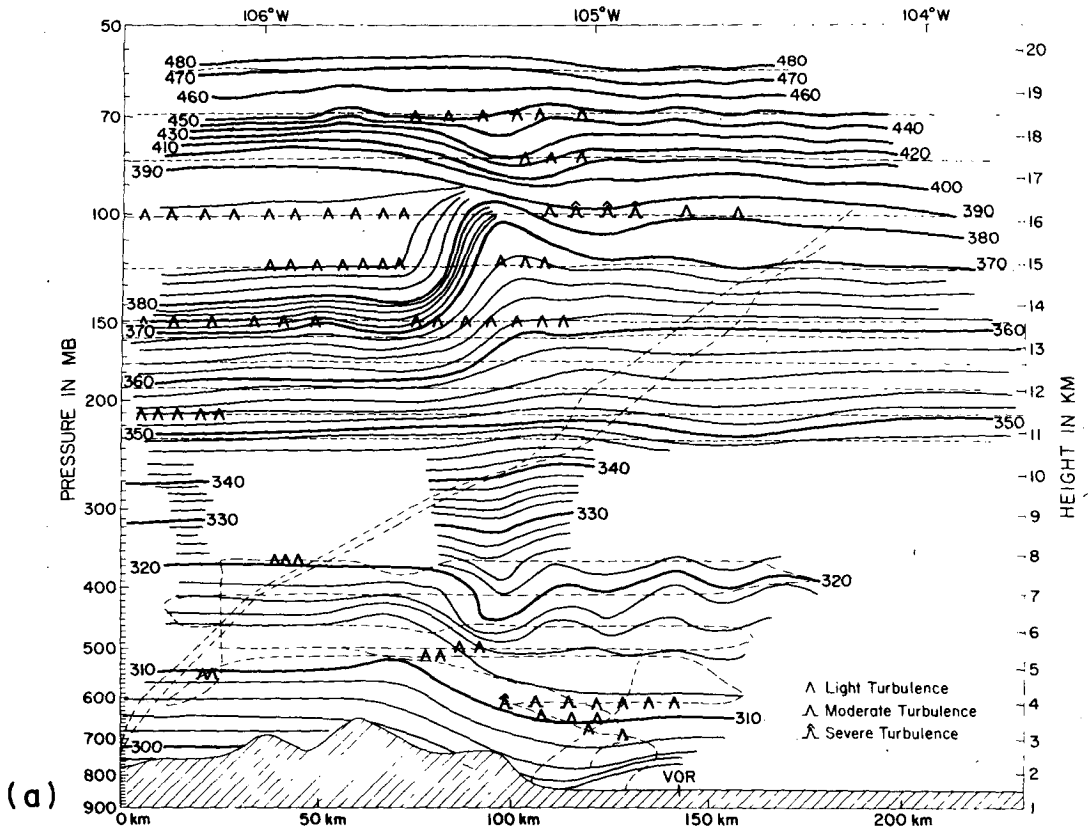
106°W
105°W
104°W
PRESSURE IN MB
HEIGHT IN KM
Light Turbulence
Moderate Turbulence
Severe Turbulence
VOR
0 km
50 km
100 km
150 km
200 km

(a)

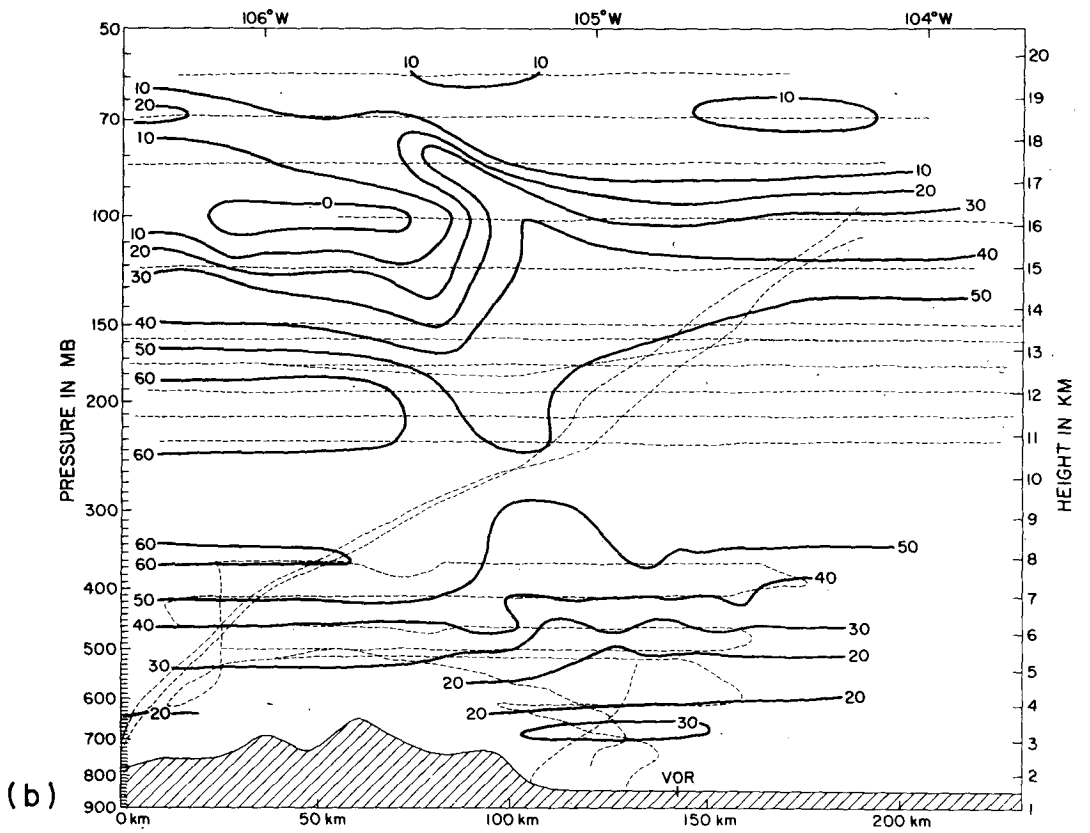
106°W
105°W
104°W
PRESSURE IN MB
HEIGHT IN KM
VOR
0 km
50 km
100 km
150 km
200 km

(b)

In the linear case, the base of the upwind sounding was taken at 700 mb and the mountain contour was specified using a ramp profile as suggested by the upwind structure of the observed low-level θ surfaces. Since a linear model precludes any upstream influence caused by a finite mountain height, this procedure attempted to roughly account for this effect by choosing the upwind surface level near the height of the Continental Divide. Computing the linear solution based on the sounding taken down to 830 mb, as used to obtain Fig. 15, produced a small-amplitude wave; including the portion of the sounding below mountain-top level caused the phase shift across the troposphere to increase from an optimal value near one-half of a vertical wavelength to 0.8 which is usually associated with a weak response (see Klemp and Lilly, 1975). On the other hand, using a sounding base of 700 mb in the nonlinear model, the wave no longer maintained its position immediately in the lee of the mountain. Rather it moved downstream in a manner somewhat similar to a propagating jump. Thus, at least for this particular nonlinear simulation, including the region of weak flow beneath the stable layer apparently reduces the low-level Froude number sufficiently to prevent significant downstream propagation of disturbances. These results suggest that regions upwind of and below the mountain crest should perhaps be omitted in linear simulations if upstream influence is thought to be significant, but in any event should be included for nonlinear modeling.

A second observational case chosen for comparison occurred on 17 February 1970. The observations were analyzed in detail by Lilly and Kennedy (1973) who presented the wave structure shown in Fig. 16. This situation is quite different from one just discussed in that strong surface winds are not present (though they did occur several hours earlier) and the hydrostatic wave appears to reach appreciable amplitude only near the tropopause. The periodic waves visible in Fig. 16a around 400 mb are probably nonhydrostatic resonant waves (see, e.g., Alaka, 1960) and cannot be represented by the model.

Since the aircraft data were accumulated between 0600 and 1000 MST, the Grand Junction sounding taken at 0500 MST on this day is well suited for initialization of the model. In addition, this sounding (shown in Fig. 17) is in approximately the correct upwind direction, as indicated by the nearly westerly flow. Sounding data were put into the model by the same procedure described for the previous case. Here potential temperature and wind profiles were specified from 830 mb to the very high and cold tropopause

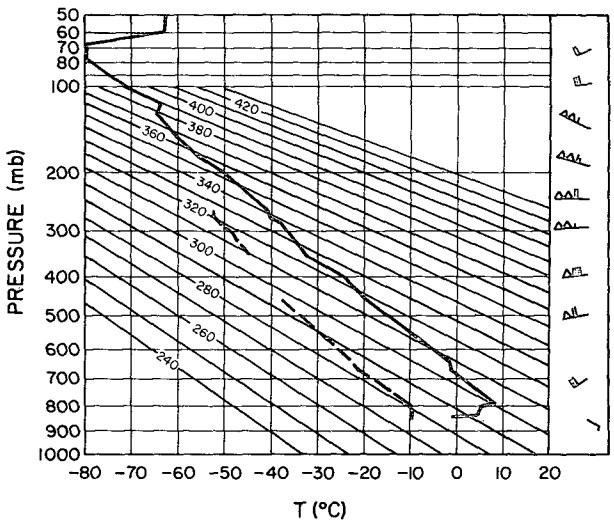

FIG. 17. Grand Junction sounding at 0500 MST 17 February 1970 (as in Fig. 14).

at about the 80 mb level. Above 80 mb the sounding was continued an additional 10 km using a constant temperature and a 10 m s^{-1} wind. Note that in the sounding below 800 mb the air is very stable with easterly flow. Since this surface inversion is probably not representative of flow passing over the mountains we chose to estimate the profiles between 830 and 800 mb from the data above 800 mb. Thus, at the base of the sounding we specified $\theta_0 = 299$ K and $u_0 = 8$ m s^{-1}.

The numerical simulation produced from this sounding data is shown in Fig. 18, and compares favorably with the observations in Fig. 16. The wave just below the tropopause is reversed in phase from the low-level flow and has comparable amplitude to the observed wave. Upstream of the upper wave, the flow is apparently blocked, and this stagnant region is also well-represented by the numerical solution. Notice that the position of the wave and the associated blocked layer in the model are about 1 km too high. This may occur because the wind speeds in the mid-troposphere are slightly too high. Consequently the vertical wavelength is increased and the position of phase reversal is somewhat elevated.

From the observations, Lilly and Kennedy (1973) also computed the vertical flux of horizontal momentum using several different techniques. The momentum flux profile derived by averaging the various approaches is depicted in Fig. 19 along with the momentum flux computed from the numerical simulation. Flux values from the model were obtained by calculating the total momentum flux (dyn cm^{-1}) across

FIG. 16a. Potential temperature cross section for 17 February 1970. Solid lines are isentropes (K), dashed lines are aircraft or balloon flight trajectories. The cross section is along a 275°–095° true azimuth line, crossing the Kremmling, Colo., and Denver VOR aircraft navigation stations. FIG. 16b. Westerly wind component cross section for 17 February 1970. Isotachs are in m s^{-1}.

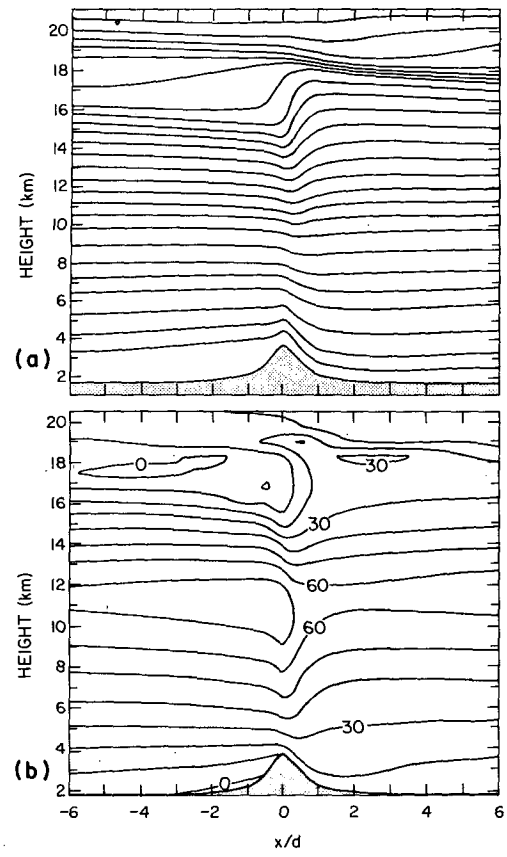

FIG. 18. Numerical simulation of 17 February 1970 case. (a) Displacement of potential temperature surfaces; (b) contours of west wind component (m s^{-1}).

each θ surface and then dividing the results by the same averaging distance (200 km) as used in computing the observational flux density. The magnitude of the simulated momentum flux is similar to observed values throughout the troposphere and then drops off sharply just below the tropopause. This decline occurs slightly above the observed turbulent layer since, as mentioned above, the position of the computed wave is slightly elevated.

This rapid decrease of momentum flux in the model occurs in the essentially inviscid domain, below the lower boundary of the damping layer located at 18 km. In this region, we would normally expect a relatively constant momentum flux profile. However, for this case the stagnant region in the upwind portion of the wave between 17 and 18 km (see Fig. 18b) forms a critical layer for stationary wave modes in which one would expect momentum removal from the mean flow. Although the critical layer does not extend across the entire domain its presence may nonetheless serve to absorb a significant amount of wave energy propagating up from below.

This situation is rather difficult to interpret since the critical layer itself is generated by the wave dynamics. To test the model behavior for a conceptually simpler case we return to a two-layer structure in which a 6°C km^{-1} lapse rate exists up to 10 km with isothermal conditions above. For the wind profile we specify a linear shear from 20 m s^{-1} at the surface to -20 m s^{-1} at 10 km, and a constant -20 m s^{-1} wind in the isothermal region. For simplicity the lateral boundaries were set periodic at $x/d=\pm 6$.

The flow structure and accompanying momentum flux profile produced by this simulation are shown in Figs. 20 and 21. Approaching the critical layer from below, the wave amplitude and momentum flux diminish rapidly; above this layer little wave motion remains and the small momentum flux has switched sign because of the change in direction of the wind. In this solution the wave breakdown which occurs in the vicinity of the critical layer cannot be modeled explicitly and thus the turbulent adjustment procedure described in Section 2e is used to parameterize this effect. In this manner small vertical scales are eliminated as the local Richardson number drops below 0.25.

If the flow were linear, the critical layer absorption would take place without reflection (Booker and Bretherton, 1967). Consequently, the low-level momentum flux should be the same as that for a one-layer radiating solution based on the atmospheric properties near the ground. (If the mean state Richardson number is much greater than unity the influence of shear on the momentum flux can be

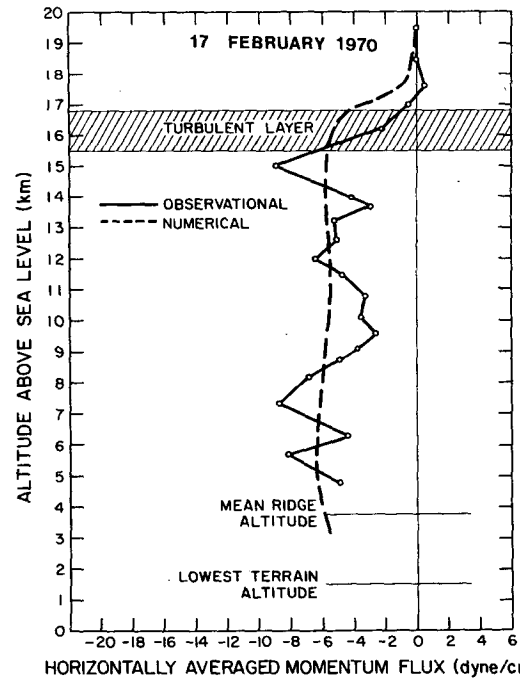

FIG. 19. Momentum flux profiles for 17 February 1970 case [solid line, observed flux profile, obtained by averaging results from several different methods of computation (see Lilly and Kennedy, 1973); dashed line, flux profile from numerical simulation].

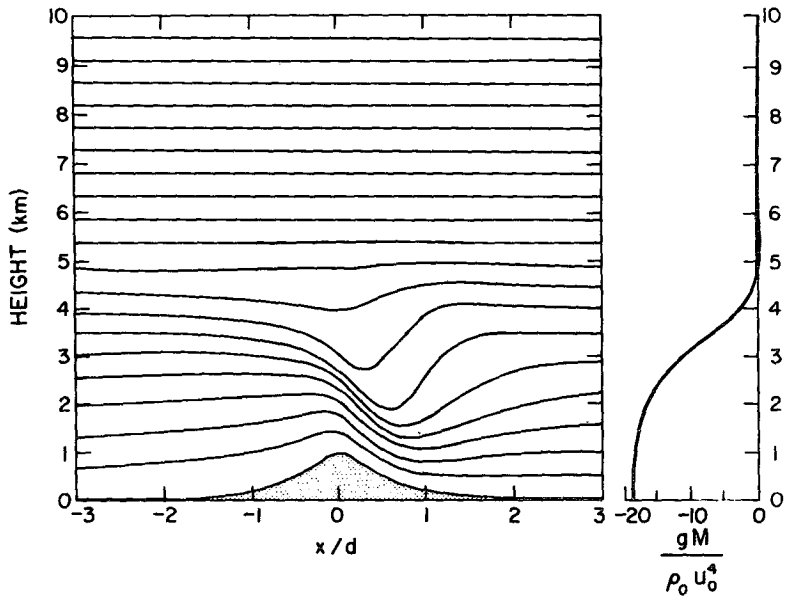

FIG. 20. Displacement of potential temperature surfaces in critical layer simulation. Initial height of critical layer is at 5 km. At right, corresponding momentum flux profile is displayed.

neglected.) For this case such a computation leads to a dimensionless momentum flux of about 11. By utilizing artificial viscosity near the critical layer, linear solutions were obtained which reproduced this theoretical value for the low level flux. Changing the magnitude of damping near the critical layer altered the flow structure in that region, but the low-level solution was unaffected. These results therefore support the linear critical layer theory by indicating little reflection. In the nonlinear solution shown in Fig. 20, however, the surface momentum flux is nearly double the linear value, implying that substantial partial reflections of the wave may be occurring. (Partial reflection of wave energy may either enhance or diminish the net momentum flux depending on the relative phase of upward and downward propagating modes.) This result is consistent with those of Breeding (1971) who found in nonlinear critical layer simulations that considerable wave energy could be reflected. If reflections occur in the vicinity of the critical level the resulting low-level momentum flux may depend on the particular approach used for parameterization of the regions of wave breakdown. For this reason we cannot justify our quantitative results for the nonlinear critical layer solution. At least qualitatively, however, the model appears to simulate the salient features of mountain wave generation in the vicinity of a critical level.

6. Summary and conclusions

In this paper we have investigated the essential features of a model designed to simulate stratified flow over finite-amplitude topographic features with reasonable accuracy. We have not considered three-dimensional flows, although we believe most of our results will extend to three-dimensional models. We have also neglected latent heat exchanges [treated to some degree by Fraser *et al.* (1973)] and lower boundary layer effects (which will, however, be reported on subsequently). In addition, we have confined our investigation to scales not significantly affected by either nonhydrostatic forces or earth's rotation, i.e., wavelengths between $2\pi\bar{u}/N$ and $2\pi\bar{u}/f$, or roughly between 10 and 1000 km.

In general we found that two of the most important modeling requirements are control over internal dissipation and an ability to simulate a radiative upper boundary condition. Without these features the predicted wave response will tend to be unstable or overdamped, and will incorrectly predict the vertical momentum flux, surface wind amplitude and the vertical structure of all fields. We found that nonlinear solutions are best represented using "open" lateral boundary conditions, as described in Section 2, though results which do not exhibit significant blocking could be obtained with cyclic lateral conditions. We do not believe that highly stretched lateral grids are useful for avoiding the need for lateral boundaries, because of their tendency to cause aliasing problems, spurious reflection and possibly instability. Our use of potential temperature coordinates and our turbulent adjustment procedure seem efficient but not essential. The latter could be replaced by some form of viscosity with strong Richardson number dependence.

In transferring our model specifications to a three-dimensional framework, the most serious problems

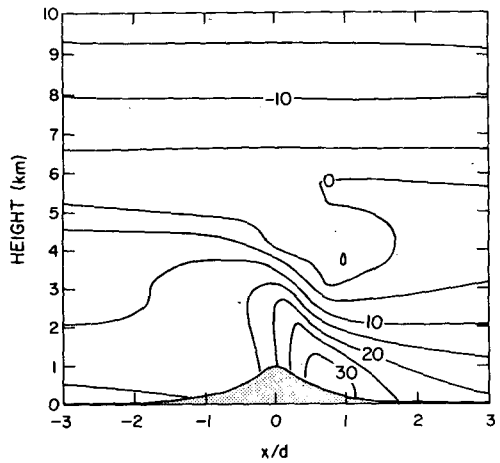

FIG. 21. Contours of horizontal velocity (m s^{-1}) for critical layer simulation depicted also in Fig. 20.

would probably arise in the upper boundary condition. Our recommendations of at least one vertical wavelength of damping, consisting of eight grid points and a nominal Reynolds number of order 1, would require a burdensome increase in the size of the integration domain and could in fact be impossible to accommodate if the wind speed and dominant forcing scale are varying with space and time over a substantial range of magnitudes. While it may be possible to vary the viscosity profile locally, it is hard to see how the dimensions of the damping layer itself could be so readily adjusted. Of course the optimal solution would be to apply a mathematical radiation condition along the upper boundary in a form which is stable and efficient for a time-dependent nonlinear framework. Such a formulation clearly requires a nonlocal specification of conditions.

The results of our numerical experiments with idealized profiles and mountain shapes appear consistent with accepted wave theory, but extend to cases where analytic theory is cumbersome or unavailable. In conventional analyses, one of the first effect of nonlinearity in forced gravity waves arises in the boundary conditions. This effect is demonstrated by comparison of linear solutions in height and potential temperature coordinates, since the boundary conditions in the latter case remain correct for finite amplitude topography. In this regard, linear solutions in a terrain following coordinate are superior to those in the (x,z) framework. For still larger amplitude forcing, nonlinear effects are exhibited in the development of upstream influence (blocking), secondary flow instability (shearing and resonant interaction) and jumplike phenomena, but the order of appearance of these phenomena depends on details of the upstream flow profiles and the topographic forcing. For reasons that remain somewhat unclear, the existence of nonlinear effects can lead to slowly varying temporal fluctuations which inhibit complete convergence to a steady-state solution. It seems possible that some of the characteristic variability in the intensity of wave-induced downslope windstorms may be associated with these effects.

The application of our model to real data cases produced two rather noteworthy results. For the 11 January 1972 windstorm the basic flow structure is well-represented by the model, though the momentum flux amplitude was some 30% lower than observed. The results also help to justify certain procedures used in our attempts to predict downslope windstorms using linear theory. In general, we have found it appropriate to specify the mean state in the linear model using only the portion of the upstream sounding above a level of 700 mb, about 50 mb below the mountain ridge crest. Our assumption, based in large part on a few well-documented aircraft flight profiles, was that the flow below this level was blocked and/or diverted around the mountain range, and thus could not contribute to the windstorm dynamics. Our nonlinear model, however, is initialized using the entire upstream sounding profile. In this case the upstream blocking develops naturally and apparently correctly, without the need for three-dimensional diversion of the low-level flow around the mountain range. The flow simulation for the 11 January storm is also successful in reproducing the strong winds immediately in the lee of the mountain and the intense shear layer in the mid-troposphere which led to severe turbulence for aircraft crossing the Rockies on that day.

The numerical results for the 17 February 1970 data show a striking resemblance to observed data. The apparent existence of an elevated region of blocking near the tropopause was simulated quite accurately by the model, as was one of the more puzzling features of the analysis, the almost complete absorption of the wave energy in this region. While we still do not fully understand this result, the absorption appears to result from a combination of the elevated upstream block providing at least a partial critical layer and downstream flow instability due to large shear. In addition, the model predicted a momentum flux profile essentially identical to that observed.

Finally, our preliminary investigation of model solutions with the presence of a more conventional critical layer suggests that for nonlinear waves, critical layers may produce considerable wave reflection which may strongly influence low-level wave characteristics. The magnitude and phase of this reflection, however, may be strongly dependent on details of the parameterized mechanism for turbulent energy dissipation. Consequently, further investigation of the dissipation mechanism is warranted if one seeks quantitatively accurate critical layer solutions.

APPENDIX

Analysis of Lateral Boundary Conditions

The lateral boundary conditions presented in Section 2c appear to be numerically stable and to cause little reflection for the mountain wave problem. To provide some justification for these boundary conditions, we present here an analysis of the boundary reflection for the linearized equations. In evaluating the reflection at the lateral boundaries we are aided by the fact that for each vertical wavenumber l, the linear equations (13) are identical in form to the two-dimensional shallow water equations. Thus the hydrostatic equations can be analyzed by considering boundary conditions for the simpler shallow water equations, assuming the speed of wave propagation is not precisely known (being dependent upon l). Nonreflective boundary conditions can be specified for the shallow water equations when the wave speed is known by setting the amplitude of the incoming characteristic equal to zero. Consequently, we shall evaluate the reflection caused by improperly estimating the wave speed.

For this analysis boundary reflection is evaluated for incident disturbances which are periodic both in space and time, and thus reflected modes are also periodic. Although these perturbations are greatly oversimplified, they can be considered to be individual Fourier components of actual disturbances. Evidence will subsequently be provided to verify that the results from this approach agree well with observed reflection in numerical simulations.

Assuming perfect temporal resolution and using second-order finite differences for the spatial derivatives, the vertically transformed equations (13) become

$$\left.\begin{aligned} &\frac{\partial \hat{u}}{\partial t}+\bar{u}\delta_{2x}\hat{u}+\delta_{2x}\hat{\Phi}=0 \\ &\frac{\partial \hat{\Phi}}{\partial t}+\bar{u}\delta_{2x}\hat{\Phi}+c^2\delta_{2x}\hat{u}+0 \end{aligned}\right\}, \tag{A1}$$

which are identical to the shallow water equations if we identify $\hat{u}$ with u and $\hat{\Phi}$ with gh. Seeking periodic solutions to (A1) we find two physical wave modes of the form

$$\text{I:}\quad (\hat{u}_1,\hat{\Phi}_1)=(u_1,\Phi_1)e^{i(k_1x-\omega_1t)},$$
$$\omega_1=[(\bar{u}+c)/\Delta x]\sin k_1\Delta x, \tag{A2}$$

$$\text{II:}\quad (\hat{u}_2,\hat{\Phi}_2)=(u_2,\Phi_2)e^{i(k_2x-\omega_2t)},$$
$$\omega_2=[(\bar{u}-c)/\Delta x]\sin k_2\Delta x. \tag{A3}$$

The expressions for ω_1 and ω_2 are required for modes I and II to be solutions of (A1). Because (A1) are finite-difference equations, two computational modes can also exist which are solutions to (A1). These are

$$\text{III:}\quad (\hat{u}_3,\hat{\Phi}_3)=(u_3,\Phi_3)e^{i(k_3x-\omega_1t)},$$
$$\omega_1=[(\bar{u}+c)/\Delta x]\sin k_3\Delta x, \tag{A4}$$

$$\text{IV:}\quad (\hat{u}_4,\hat{\Phi}_4)=(u_4,\Phi_4)e^{i(k_4x-\omega_2t)},$$
$$\omega_2=[(\bar{u}-c)/\Delta x]\sin k_4\Delta x, \tag{A5}$$

and are related to the physical modes by

$$k_3=\frac{\pi}{\Delta x}-k_1,\quad k_4=\frac{\pi}{\Delta x}-k_2. \tag{A6}$$

In other words, there are two horizontal wavenumbers corresponding to each value of the frequency, a physical mode and a computational mode. As $\omega\to 0$ the physical mode approaches infinite wavelength, while the computational mode approaches $2\Delta x$. The group velocities $(\partial\omega/\partial k)$ of the disturbances are given by

$$\left.\begin{aligned} c_{g1}&=-c_{g3}=(\bar{u}+c)\cos k_1\Delta x \\ c_{g2}&=-c_{g4}=(\bar{u}-c)\cos k_2\Delta x \end{aligned}\right\}, \tag{A7}$$

and thus two modes propagate upstream and two downstream regardless of the magnitude of c. For the present analysis we shall not be concerned with the effects of limited resolution and thus we assume $k_1\Delta x\ll 1$ and $k_2\Delta x\ll 1$. Under these conditions, the computational mode wavelengths are approaching $2\Delta x$. For $c>\bar{u}$, one physical and one computational mode propagate upstream and one of each travel downstream; for $c<\bar{u}$, both physical modes move downstream and only the computational modes propagate upstream.

Turning to the outflow boundary we first consider the case $c>\bar{u}>0$ implying one physical mode can propagate upstream and thus one boundary condition should be specified. For this situation mode I is the incident physical mode. If a boundary condition is specified which is not compatible with this disturbance, reflection can take place into physical mode II and/or computational mode III since they have group velocities directed upstream. For the solution to remain continuous, the frequencies of the incident and reflected modes must match at the boundary. By setting $\omega_1=\omega_2$, we obtain

$$k_2=k_1\left(\frac{\bar{u}+c}{\bar{u}-c}\right) \tag{A8}$$

and consequently reflection into the physical mode from the outflow boundary always occurs with higher wavenumber than the incident mode. In (A8) it is assumed $\sin k\Delta x\approx k\Delta x$. If the resolution is limited this approximation may not be valid. In fact, if $(\bar{u}+c)/(\bar{u}-c)\sin k_1\Delta x$ exceeds unity, k_2 becomes complex and causes the reflected modes to be exponentially damped out as they propagate upstream.

To evaluate the reflection caused by a particular boundary formulation, we define a reflection coefficient, $r_{ij}=|u_i/u_j|$, which represents the ratio of the reflected wave amplitude to that of the incident mode. For this situation, r_{21} is the coefficient for the reflected physical mode while r_{31} corresponds to the computational mode.

As mentioned above, for $c>\bar{u}$ one boundary condition should be specified at the outflow boundary. Thus, at outflow we replace the momentum equation with a specified boundary condition for $\hat{u}$ and solve the $\hat{\Phi}$ equation using first-order one-sided differences for the spatial derivatives. (Because of the symmetry of the equations, the same results would be obtained if the boundary condition was specified for $\hat{\Phi}$ instead of $\hat{u}$.) For any particular boundary condition the reflectivity is obtained by substituting $\hat{u}=\hat{u}_1+\hat{u}_2+\hat{u}_3$ and $\hat{\Phi}=\hat{\Phi}_1+\hat{\Phi}_2+\hat{\Phi}_3$ into the two boundary equations and solving for r_{21} and r_{31}. This procedure is essentially the same as that used by Nitta (1964) and Matsuno (1966) in analyzing outflow boundary conditions. Deriving these solutions for several possible boundary conditions yields the following results for physical mode reflection:

Outflow boundary condition	r_{21}	
$\hat{u}_N=0$	1	(A9)
$\hat{u}_N=\hat{u}_{N-1}$	$\left\|\frac{\bar{u}-c}{\bar{u}+c}\right\|$	(A10)
$\hat{u}_N=2\hat{u}_{N-1}-\hat{u}_{N-2}$	$\left\|\frac{\bar{u}-c}{\bar{u}+c}\right\|^2$	(A11)
$\frac{\partial\hat{u}}{\partial t}+\frac{\bar{u}}{\Delta x}(\hat{u}_N-\hat{u}_{N-1})=0$	$\left\|\frac{\bar{u}-c}{\bar{u}+c}\right\|$	(A12)
$\frac{\partial\hat{u}}{\partial t}+\frac{\bar{u}+c_0^*}{\Delta x}(\hat{u}_N-\hat{u}_{N-1})=0$	$\left\|\frac{(\bar{u}-c)}{(\bar{u}+c)}\frac{(c-c_0^*)}{(c+c_0^*)}\right\|$	(A13)

Here $\hat{u}_{N-i}$ is the value of $\hat{u}$ at i grid points in from the boundary. In all cases since the correct number of conditions has been specified, reflection into the computational mode is $O[(k_1\Delta x)^2]$.

Condition (A9) gives the expected result that if one of the two variables is held fixed total reflection will occur. Conditions (A10)–(A12) are ones which might be considered for limited area modeling and produce reflection amplitudes dependent upon the relative magnitudes of $\bar{u}$ and c. For $\bar{u}\to 0$ each of these conditions becomes completely reflective.

The boundary condition chosen for use in the wave model is given by (A13). This condition attempts to advect the variable out at an estimated phase speed of the wave, $\bar{u}+c_0^*$. For $c=c_0^*$, Eq. (A13) is consistent with setting the amplitude of the incoming characteristic, η in (14), equal to zero. In fact, (A13) can be derived from (14) by setting $\eta=0$, which implies $\zeta=2u$ at the boundary. The second term in r_{21} reduces the reflection amplitude with increasing effectiveness as the estimated intrinsic phase speed c_0^* approaches the actual phase speed c. Even for phase speeds which are not particularly close to c_0^*, r_{21} is likely to be significantly less than unity.

As mentioned above the shallow water equations describe the behavior for a single vertical mode in the hydrostatic system. Although many such modes may exist in a particular physical situation, only one value of c_0^* can be used in the formulation. Suppose we choose $c_0^*>\bar{u}$ to handle the dominant modes in the system, but other modes are also present having shorter vertical wavelengths such that $c<\bar{u}$. For waves having $c<\bar{u}$, both physical modes propagate downstream and hence no outflow boundary condition should be specified. By imposing (A13) at this boundary, reflection occurs into both computational modes which then travel upstream as indicated by (A7). The amplitude of these modes is determined from the same procedure used in deriving (A9)–(A13). Here, the incident and reflected modes are substituted into (A13) and the boundary equation for $\hat{\Phi}$ and the two equations are solved for the reflection coefficients of the two computational modes. For mode I incident upon the boundary this procedure yields

$$r_{31}=\left|\frac{k_1\Delta x}{4}\frac{(\bar{u}-c)(c-c_0^*)}{\bar{u}(\bar{u}+c_0^*)}\right|,\qquad r_{41}=\left|\frac{k_1\Delta x}{4}\frac{(\bar{u}+c)(c-c_0^*)}{\bar{u}(\bar{u}+c_0^*)}\right|, \tag{A14}$$

while for mode II incident we have

$$r_{32}=\left|\frac{k_2\Delta x}{4}\frac{(\bar{u}+c)(c+c_0^*)}{\bar{u}(\bar{u}+c_0^*)}\right|,\qquad r_{42}=\left|\frac{k_2\Delta x}{4}\frac{(\bar{u}-c)(c+c_0^*)}{\bar{u}(\bar{u}+c_0^*)}\right|. \tag{A15}$$

In deriving these expressions, we have assumed $e^{\pm ik\Delta x}\approx 1\pm ik\Delta x$ for the incident modes. Having incorrectly specified a boundary condition for these modes, reflection into the computational modes is now $O(k\Delta x)$ instead of $O[(k\Delta x)^2]$. However, if the resolution of the incident modes is sufficiently high (i.e., $k\Delta x\ll 1$), reflected computational modes will remain small amplitude. Furthermore, any small background damping present in a numerical model will efficiently remove these high wavenumber disturbances.

At the inflow boundary we again consider wave modes for which $c>\bar{u}$ since for $c<\bar{u}$ the modes will not propagate upstream to reach this boundary. For

this situation mode II given by (A3) is the incident wave and mode I represented by (A2) is the reflected physical mode. Since the frequencies of incident and reflected modes must again match at the boundary the wavenumber k_1 of the reflected physical mode is determined from (A8). Thus, at the inflow boundary the reflected physical mode will have a longer wavelength than the corresponding incident mode.

For $c>\bar{u}$ one physical mode propagates in each direction and, consequently, one boundary condition should be specified at the inflow boundary. However, this specification is complicated by the fact that both equations in (A1) must be altered or replaced since the advection term in each equation cannot be represented using a one-sided finite difference at the boundary. As a result we seek to specify one condition which can be used to alter both equations. By again estimating an intrinsic phase speed c_0^* of the wave the momentum equation is replaced by

$$\frac{\partial \hat{u}}{\partial t}+(\bar{u}-c_i^*)\frac{\partial \hat{u}}{\partial x}=0. \tag{A16}$$

By requiring $\bar{u}-c<0$ the spatial derivative in (A16) can be stably represented with a one-sided finite difference. Note that (A16) can be derived from the momentum equation if we set $\hat{\Phi}_x=-c_i^*\hat{u}_x$. If we use this relationship to eliminate the advection term in the $\hat{\Phi}$ equation, computational mode reflection is $r_{42}=O[(k_2\Delta x)^2]$ but the physical mode reflection becomes

$$r_{12}=\left|\frac{(\bar{u}+c)}{(\bar{u}-c)}\frac{(c-c_i^*)}{(c+c_i^*)}\right|. \tag{A17}$$

This result is unacceptable since the first term in (A17) can be large. To reduce r_{21}, we alter the $\hat{\Phi}$ equation at the boundary by assuming

$$\frac{\partial \hat{\Phi}}{\partial t}=-\bar{u}\frac{\partial \hat{\Phi}}{\partial x}+c^2\frac{\partial \hat{u}}{\partial x}=(\bar{u}-c_i^*)\frac{\partial \Phi}{\partial x}. \tag{A18}$$

This expression is correct for $c_i^*=c$, but slightly overspecifies conditions at the boundary when c is not precisely known. Rather than solve the right hand part of (A18) as a prognostic equation for $\hat{\Phi}$, we only use (A18) to eliminate the advection term in the $\hat{\Phi}$ equation. Solving (A18) for $\hat{\Phi}_x$,

$$\frac{\partial \hat{\Phi}}{\partial x}=-\frac{c^2}{c_i^*}\frac{\partial \hat{u}}{\partial x}$$

allows the boundary equation for $\hat{\Phi}$ to be written as

$$\frac{\partial \hat{\Phi}}{\partial t}+\left(1-\frac{\bar{u}}{c_i^*}\right)c^2\frac{\partial \hat{u}}{\partial x}=0. \tag{A19}$$

The reflectivity of these boundary equations can be determined using the same techniques as described for the outflow boundary and yields reflection coefficients for the physical mode r_{12} and the computational mode r_{42} given by

$$r_{12}=\left|\frac{c-c_i^*}{c+c_i^*}\right|,\quad r_{42}=\left|\frac{k_2\Delta x\bar{u}(c-c_i^*)}{(\bar{u}+c)(\bar{u}-c_i^*)}\right|. \tag{A20}$$

Contrary to (A17), r_{21} in (A20) is always less than unity and vanishes as c^* approaches c. Although the computational mode r_{42} is now $O(k_2\Delta x)$, the coefficient multiplying $k_2\Delta x$ is likely to be much less than unity and it vanishes as $\bar{u}\to 0$ or $c_i^*\to c$. Eq. (A20) indicates, however, that if any modes can propagate upstream c_i^* must not be set equal to $\bar{u}$.

The above analyses consider the reflection of a physical wave mode incident upon either an inflow or outflow lateral boundary. However, amplification of reflected modes can also occur through subsequent reflections as disturbances propagate back and forth across the domain. For example, if the physical mode I is incident upon the outflow boundary and produces some reflection into mode III, this computational mode will propagate upstream and reflect off the inflow boundary, regenerating modes I and IV which then propagate back downstream. With the inflow boundary conditions described above the reflection coefficients for these two modes (derived using the same procedure as used for reflection of the physical modes) are both O(1) in magnitude. Thus computational modes generated at the outflow boundary will not amplify upon reflection at the inflow boundary. Secondary reflections at the outflow boundary are potentially more troublesome. If computational mode IV (produced originally at the inflow boundary) impinges upon the downstream boundary, the boundary condition (A13) causes O(1) reflection into the computational mode III. However, reflection into the physical mode II becomes

$$r_{24}=\left|\frac{1}{k_2\Delta x}\frac{(\bar{u}+c_0^*)}{(\bar{u}+c)}\frac{(c-c_0^*)}{(c+c_0^*)}\right|=O[(k\Delta x)^{-1}]. \tag{A21}$$

Thus the amplitude of this physical mode relative to the original wave amplitude impinging upon the upstream boundary is given by the product of r_{24} from (21) and r_{42} from (A20). Although this product is O(1), its amplitude should be small since both coefficients vanish as c_i^*, $c_0^*\to c$. In addition, any small background damping in the domain will preferentially reduce computational mode amplitudes as they propagate across the domain due to their high wavenumber.

In the above analyses we have assumed good resolution of the physical modes in the system. If disturbances are present which are not adequately resolved by the finite-difference equations, reflectivity at the boundary will increase. This enhancement of reflection with diminished resolution appears to be a fundamental problem and not associated with just a particular set of boundary formulations. For example, in the shallow-water equations where c is precisely

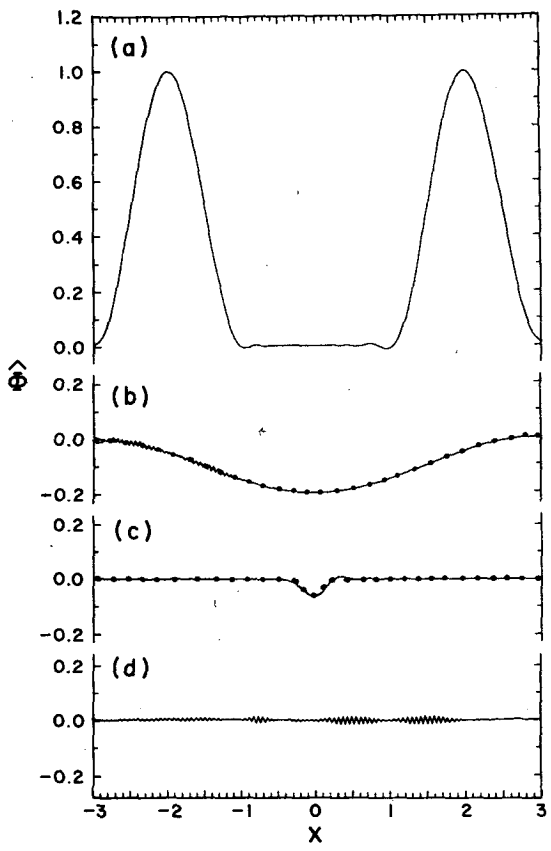

FIG. A1. Boundary reflection in shallow water equations. (a) Incident wave modes with $\bar{u}=10$ m s^{-1}, $c=20$ m s^{-1}; (b) reflected wave from inflow boundary for $c^*=30$ m s^{-1}; (c) reflected wave from outflow boundary for $c^*=30$ m s^{-1}; (d) reflected computational mode for $\bar{u}=20$ m s^{-1}, $c=10$ m s^{-1} and $c^*=30$ m s^{-1}.

known, boundary conditions which are mathematically nonreflective produce reflection into the computational mode which approaches unity as the incident mode wavelength tends to $4\Delta x$. This reflection is caused by the one-sided difference taken at the boundary.

The expressions for boundary reflectivity have been derived by analyzing incident and reflected disturbances which are continuously periodic in both time and space. To demonstrate that these results apply to finite nonperiodic disturbances, Eqs. (A1) were numerically integrated with the lateral boundary conditions specified as described above. Using dimensionless variables an initial perturbation for $\hat{\Phi}$ is specified by

$$\hat{\Phi}(x,0)=\begin{cases}2\cos^2[(\pi/2)(x+1)], & -2<x<0\\ 0, & x\leqslant -2,\ x\geqslant 0.\end{cases} \tag{A22}$$

The mean wind speed $\bar{u}$ is 10 m s^{-1}, the phase speed c is 20 m s^{-1} and the lateral boundaries are placed at $x=\pm 3$. The horizontal grid interval is $\Delta x=0.03$. Integrating forward in time using a leapfrog procedure, this initial profile produces two perturbations of unit amplitude; one propagates upstream at $\bar{u}-c=10$ m s^{-1} while the other moves downstream at $\bar{u}+c=30$ m s^{-1}. These disturbances are shown in Fig. A1a at a dimensionless time of $\bar{u}t/d=1$, where L is the length scale used to render x dimensionless. Recalling the application of this analysis to the hydrostatic problem (where a number of phase speeds may exist simultaneously) we examine the effect of incorrectly estimating c^* by setting $c^*=30$ m s^{-1}.

To isolate the reflection at each boundary two separate simulations were computed. In the first we specified $c_i^*=30$ m s^{-1} at the inflow boundary and $c_0^*=20$ m s^{-1} at outflow. For this case virtually all reflection is generated at the inflow boundary and Fig. A1b depicts the solution at a time ($\bar{u}t/d=3$) when the reflected physical mode has propagated into the middle of the domain. The corresponding dotted line represents the theoretical result based on the periodic analysis and is virtually coincident with the numerical solution. The analytic solution is obtained by specifying the following characteristics for the reflected physical mode: a horizontal scale exactly three times that of the incident wave from (A8), an amplitude equal to 20% of the incident wave from (A20), and a propagation speed of 30 m s^{-1} from (A7). The small-scale oscillations near the inflow boundary are small-amplitude computational modes nearly $2\Delta x$ in wavelength produced according to (A20).

In the second simulation we evaluate reflection from the downstream boundary by setting $c_i^*=20$ m s^{-1} at inflow and at $c_0^*=30$ m s^{-1} for the outflow boundary condition (A13). In this situation all visible reflection emanates from the outflow boundary and is shown in Fig. A1c at a time ($\bar{u}t/d=4.4$) when the physical mode has traveled back to the center of the domain. Again the dotted line depicts the theoretical solution for the reflected physical mode which has 1/3 the wavelength [from (A8)] and 1/15 the amplitude [from (A13)] of the incident mode and travels upstream at 10 m s^{-1} [from (A7)].

These two simulations demonstrate an excellent agreement between the theoretical reflection characteristics and those actually computed. As a result we have some confidence that the analysis based on periodic modes can be applied to the finite disturbances which are of physical interest.

A final computation with the shallow water equations was performed to observe the reflection caused when (A13) is specified at the outflow boundary but both wave modes are propagating downstream. In this case the downstream boundary is overspecified and reflection takes place into the computational modes as indicated by (A14) and (A15). Here we specified $\bar{u}=20$ m s^{-1}, $c=10$ m s^{-1}, $c_0^*=30$ m s^{-1}, and initialize according to (A22). The two physical modes then propagate downstream at 30 and 10 m s^{-1}, respectively, and produce reflected computational modes which are shown in Fig. A1d one-half dimensionless time unit after the second physical mode has passed

through the boundary. From (A14) and (A15) the largest reflection coefficient should be r_{23}; by estimating a representative wavenumber in the incident disturbance as $k_2=\pi$, we compute $r_{32}=0.028$ which is similar to the maximum observed amplitudes. Thus, even though the outflow boundary conditions were not properly specified, computational mode reflection can remain small in amplitude.

Clearly, the actual reflection produced in a particular simulation will depend on the wave modes present and the chosen value of c^*. Whether c^* is estimated from the dominant scales of motion present or computed from properties of the flow field near the boundary, it can at best be considered a rough approximation to the physical modes in the system. The advantage of this approach is that the boundary formulations appear to be stable in the absence of any damping mechanisms and yield reflection coefficients which are always less than (and in many cases much less than) unity. The question as to whether or not the reflection levels are sufficiently small must of course be analyzed for the particular application under consideration.

In the above analysis we have been concerned only with the problem of letting disturbances within the model domain pass out through the boundaries. One may also wish to introduce disturbances into the domain by varying conditions at the boundary. This can be accomplished by adding a tendency term to any or all of the boundary equations to represent the time rate of change of the imposed conditions. In the linear system of equations, the modes passing out through the boundary are completely decoupled from those introduced at the boundary through tendency terms and thus the two processes have no influence on each other. This result was verified in the numerical model for the shallow water equations. At the inflow boundary time tendencies were added to both prognostic equations to produce a particular wave in the interior. At the same time a wave was propagated into the boundary from the interior. By specifying c_i^* according to the phase speed of the incident wave, the forced wave entered the domain as desired and the incident mode passed out without reflection.

REFERENCES

Alaka, M. A., Ed., 1960: The airflow over mountains. WMO Tech. Note No. 34, 135 pp.

Anthes, R. A., and T. T. Warner, 1974: Prediction of mesoscale flows over complex terrain. U. S. Army Electronic Command, Rep. ECOM-5532, 101 pp.

Blumen, W., 1965: A random model of momentum flux by mountain waves. *Geofis. Publ.*, **26**, 1–33.

Booker, J. R., and F. P. Bretherton, 1967: The critical layer for internal gravity waves in a shear flow. *J. Fluid Mech.*, **27**, 513–539.

Breeding, R. J., 1971: A nonlinear investigation of critical levels for internal atmospheric gravity waves. *J. Fluid Mech.*, **50**, 545–563.

Brinkmann, W. A. R., 1974: Strong downslope winds at Boulder, Colorado. *Mon. Wea. Rev.*, **102**, 592–602.

Davis, R. E., and A. Acrivos, 1967: The stability of oscillatory internal waves. *J. Fluid Mech.*, **30**, 723–736.

Deaven, D. G., 1976: A solution for boundary problems in isentropic coordinate models. *J. Atmos. Sci.*, **33**, 1702–1713.

Drazin, P. G., and C. H. Su, 1975: A note on long-wave theory of airflow over a mountain. *J. Atmos. Sci.*, **32**, 437–439.

Eliassen, A., and E. Palm, 1960: On the transfer of energy in stationary mountain waves. *Geofis. Publ.*, **22**, 1–23.

——, and J. Rekustad, 1971: A numerical study of meso-scale mountain waves. *Geofis. Publ.*, **28**, 1–13.

Elvius, E., and A. Sundström, 1973: Computationally efficient scheme and boundary conditions for fine mesh barotropic model based on the shallow water equations. *Tellus*, **25**, 132–156.

Foldvik, A., and M. G. Wurtele, 1967: The computation of the transient gravity wave. *Geophys. J. Roy. Astron. Soc.*, **13**, 167–185.

Fraser, A. B., R. C. Easter and P. V. Hobbs, 1973: A theoretical study of the flow of air and fallout of solid precipitation over mountainous terrain: Part I. Air flow model. *J. Atmos. Sci.*, **30**, 801–812.

Hasselmann, K., 1967: A criterion for nonlinear wave stability. *J. Fluid Mech*, **30**, 737–739

Houghton, D. D., and W. Jones, 1969: A numerical model for linearized gravity and acoustic waves. *J. Comput. Phys.*, **3**, 339–357.

Klemp, J. B., and D. K. Lilly, 1975: The dynamics of wave-induced downslope winds. *J. Atmos. Sci.*, **32**, 320–339.

——, and R. B. Wilhelmson, 1978: Numerical simulation of convective storm dynamics. Submitted to *J. Atmos. Sci.*

Krishnamurti, T. N., 1964: The finite-amplitude mountain wave problem with entropy as a vertical coordinate. *Mon. Wea. Rev.*, **92**, 147–160.

Lilly, D. K., 1972: Wave momentum flux—a GARP problem. *Bull. Amer. Meteor. Soc.*, **53**, 17–23.

——, and E. J. Zipser, 1972: The front range windstorm of 11 January 1972—a meteorological narrative. *Weatherwise*, **25**, 56–63.

——, and P. J. Kennedy, 1973: Observations of a stationary mountain wave and its associated momentum flux and energy dissipation. *J. Atmos. Sci.*, **30**, 1135–1152.

——, 1978: Analysis of an intense mountain wave and aircraft turbulence. *J. Atmos. Sci.*, **35**, 59–77.

——, and J. B. Klemp, 1977: Analytic solutions of non-linear hydrostatic mountain wave equations. Submitted to *J. Fluid Mech.*

Long, R. R., 1953: Some aspects of the flow of stratified fluids. I. A theoretical investigation. *Tellus*, **5**, 42–58.

Mahrer, Y., and R. A. Pielke, 1975: A numerical study of the air flow over mountains using the two-dimensional version of the University of Virginia mesoscale model. *J. Atmos. Sci.*, **32**, 2144–2155.

Matsuno, T., 1966: False reflection of waves at the boundary due to the use of finite differences. *J. Meteor. Soc. Japan*, **44**, 145–157.

Nichols, J. M., 1974: The airflow over mountains—research 1958–1972. WMO Tech. Note No. 127, 73 pp.

Nitta, T., 1964: On the reflective computational wave caused by the outflow boundary condition. *J. Meteor. Soc. Japan*, **42**, 274–276.

Oliger, J., and A. Sundström, 1976: Theoretical and practical aspects of some initial boundary value problems in fluid dynamics. Stanford University Computer Sci. Dept. Rep. STAN-CS-76-578, 61 pp.

Orlanski, I., 1976: A simple boundary condition for unbounded hyperbolic flows. *J. Comput. Phys.*, **21**, 251–269.

Smith, R. B., 1977: The steepening of hydrostatic mountain waves. *J. Atmos. Sci.*, **34**, 1634–1654.